



Effect of internal mass in the simulation of a moving body by the immersed boundary method

Kosuke Suzuki^a, Takaji Inamuro^{a,b,*}

^a Department of Aeronautics and Astronautics, Graduate School of Engineering, Kyoto University, Kyoto 606-8501, Japan

^b Advanced Research Institute of Fluid Science and Engineering, Graduate School of Engineering, Kyoto University, Kyoto 606-8501, Japan

ARTICLE INFO

Article history:

Received 17 January 2011

Received in revised form 1 April 2011

Accepted 20 May 2011

Available online 12 June 2011

Keywords:

Internal mass effect

Immersed boundary method

Unsteady body motion

ABSTRACT

We investigate the effect of internal mass in the simulation of a moving body by the immersed boundary method. In general, the force and the torque acting on the body are influenced by the internal mass, if they are obtained by the negative of the sum of body forces which are applied near the boundary in order to enforce the no-slip condition on the boundary. In this study, the following schemes for approximating the internal mass effect are introduced; *no internal mass effect*, *rigid body approximation*, and *Lagrangian points approximation*. By comparing these schemes through the simulations of a moving body, we examine the internal mass effect. The simulations of the flow around an oscillating circular cylinder and of the sedimentations of an elliptical cylinder and a sphere are performed by using an immersed boundary–lattice Boltzmann method, and it is found that the internal mass effect is significant to unsteady body motions for the Reynolds numbers over 10 and grows as the Reynolds number increases. We also find that for the angular motions of the body, the rigid body approximation causes errors for the rotational Reynolds numbers over 10.

© 2011 Elsevier Ltd. All rights reserved.

1. Introduction

One of the important issues in computational fluid dynamics is to simulate flows around a moving body efficiently and accurately, which is called the moving boundary problem. Body-fitted or unstructured-grid methods have commonly been used to simulate the moving boundary problems. However, the algorithms of the methods are generally complicated, and also the computation costs of the methods are high. Recently, the immersed boundary method (IBM), which was proposed by Peskin [1,2] in 1970s in order to simulate blood flows in the heart, has been reconsidered as an efficient method for simulating flows around a moving body on the fixed Cartesian grid. Various approaches and applications using the IBM were reviewed by Mittal and Iaccarino [3].

In the IBM, it is assumed that a fluid is filled inside the boundary as well as outside the boundary, and then appropriate body forces are applied near the boundary in order to enforce the no-slip condition on the boundary. By the body forces, the internal fluid inside the boundary is generally moved. In general, the internal fluid does not affect the flow and the pressure outside the boundary, while the force and the torque acting on the boundary are influenced

by the internal mass, if they are obtained by the negative of the sum of the body forces following the method by Lai and Peskin [4]. However, the effect of the internal mass on the force and the torque acting on the boundary has not been investigated so much. There have been only a few studies on the effect [5–8]. ten Cate et al. [5] pointed out that the part of the force acting on the body is compensated by the change of momentum of the internal mass. Uhlmann [6] proposed an approximation of the change of momentum of the internal mass by supposing the motion of the internal mass to be a rigid body motion. However, the approximation has a limitation of the density ratio of the body to the fluid for the stable computation of the body motion. For example, the density ratio γ is required to be $\gamma \gtrsim 1.05$ for the motion of a circular disk and $\gamma \gtrsim 1.2$ for the motion of a sphere. Feng and Michaelides [7] proposed a variation of Uhlmann's approximation which does not have a limitation of the density ratio. Shen et al. [8] derived the formulation of the internal mass effect by integrating the Navier–Stokes equations with the body forces and examined the magnitude of the internal mass effect in the simulation of the drag force acting on a forced-oscillating circular cylinder in a stationary fluid. In these studies, however, there is no investigation of the effect of the internal mass in the system where the body moves freely, and also the dependency of the effect on the Reynolds number is not clear.

In this study, in order to investigate the effect of internal mass on the force and the torque acting on the body, we compare four different schemes for approximating the internal mass effect. The

* Corresponding author at: Department of Aeronautics and Astronautics, Graduate School of Engineering, Kyoto University, Kyoto 606-8501, Japan. Tel.: +81 75 753 5791; fax: +81 75 753 4947.

E-mail addresses: suzuki.kousuke@t05t92005.mbox.media.kyoto-u.ac.jp (K. Suzuki), inamuro@kuaero.kyoto-u.ac.jp (T. Inamuro).

first scheme is *no internal mass effect*, in which the internal mass effect is ignored. The second and the third schemes are *Uhlmann's rigid body approximation* and *Feng's rigid body approximation* described above. For the fourth scheme, we propose the *Lagrangian points approximation*, in which the internal mass effect is directly computed. By comparing the above four schemes through the simulations of a moving body in fluid, we investigate the magnitude of the internal mass effect on the force and the torque acting on the body and also examine the dependency of the internal mass effect on the Reynolds number.

As for the computation of viscous fluid flows, we use the lattice Boltzmann method (LBM). The lattice Boltzmann method (LBM) has been developed into an alternative and promising numerical scheme for simulating viscous fluid flows in the Cartesian grid without solving the Poisson equation for pressure field [9]. Because of its simplicity and computational efficiency as well as high scalability on parallel processing, the LBM has been applied to many simulations including moving boundary problems [10–13]. Since both of the above methods (IBM and LBM) are based on the Cartesian grid, the LBM combined with the IBM (so-called IB-LBM) is well-suited to simulations of moving boundary problems. In addition, the IB-LBM is simpler to implement on computers than the usual LBM with improved bounce back conditions on a moving boundary [15,14]. Several approaches of the IB-LBM have already been presented [12,13,16–18]. In the present paper, in order to compute viscous fluid flows including a moving body, we use an IB-LBM proposed by the authors using the Multi Direct Forcing Method (MDFM) [19] for determining body forces near the moving boundary. Unlike the original IBM by Peskin [1,2] and some variations [20], the MDFM requires no free parameters that must be chosen for implementations. Moreover, the no-slip condition on the moving boundary can be satisfied accurately by using the MDFM.

The paper is organized as follows. In Section 2 we explain the formulation of the problem based on the IBM. In Section 3 we describe the numerical method, in which the above four schemes for calculating the internal mass effect are also introduced. The simulations of a moving body are presented in Section 4. We compute the flow around an oscillating circular cylinder and the sedimentations of an elliptical cylinder and of a sphere. We finally conclude in Section 5.

2. Formulation of the problem

We consider the system where a rigid body moves in an incompressible viscous fluid.

2.1. Fluid flow with a moving body represented by the IBM

Let Ω_{all} be the entire domain of the system, $\Omega(t)$ be the closed domain inside the rigid body, and $\partial\Omega(t)$ be the surface of the body at time t (see Fig. 1). We assume that an incompressible viscous fluid with the density ρ_f is filled in the entire domain Ω_{all} , that

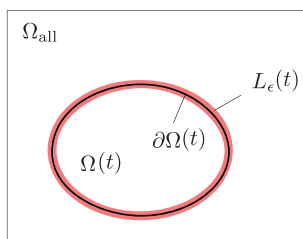


Fig. 1. The system of a moving body in a fluid represented by the IBM.

is, both inside and outside of $\Omega(t)$. We call the fluid inside $\Omega(t)$ the *internal fluid* and the fluid outside $\Omega(t)$ the *external fluid*. We assume that the no-slip condition on $\partial\Omega(t)$ is satisfied by a body force $\mathbf{g}(\mathbf{x}, t)$ applied only on the neighborhood of $\partial\Omega(t)$ defined by $L_\epsilon(t)$ which is called the *boundary shell* as shown in Fig. 1. The body force \mathbf{g} is determined by the IBM as explained in the Section 3.

The fluid flow is governed by the continuity equation and the Navier–Stokes equations as follows:

$$\nabla \cdot \mathbf{u} = 0, \quad (1)$$

$$\rho_f \left[\frac{\partial \mathbf{u}}{\partial t} + (\mathbf{u} \cdot \nabla) \mathbf{u} \right] = -\nabla p + \mu \nabla^2 \mathbf{u} + \mathbf{g}, \quad (2)$$

where $\mathbf{u}(\mathbf{x}, t)$ and $p(\mathbf{x}, t)$ are the fluid velocity and the pressure at the point \mathbf{x} at time t , and μ is the viscosity of the fluid. It should be noted that $\mathbf{g}(\mathbf{x}, t) = \mathbf{0}$ if $\mathbf{x} \notin L_\epsilon(t)$.

2.2. Body motion

We consider the motion of the rigid body with density ρ_b in $\Omega(t)$. Let the inertial reference frame be Σ_A , and the reference frame fixed to the body be Σ_B . The origin of Σ_B is placed at the center of mass of the rigid body \mathbf{X}_c . In the followings, vectors observed from Σ_B have a pre-superscript B, while vectors observed from Σ_A have no pre-superscript.

Let $\mathbf{U}_c(t)$ be the velocity of $\mathbf{X}_c(t)$, and ${}^B\boldsymbol{\Omega}_c(t)$ the angular velocity around $\mathbf{X}_c(t)$. Supposing that we obtain the force $\mathbf{F}(t)$ and the torque $\mathbf{T}(t)$ acting on the body at time t , the motion of the body is governed by the Newton–Euler equations as below:

$$M \frac{d\mathbf{U}_c}{dt} = \mathbf{F}, \quad (3)$$

$$\mathbf{I}_B \frac{d{}^B\boldsymbol{\Omega}_c}{dt} + {}^B\boldsymbol{\Omega}_c \times (\mathbf{I}_B {}^B\boldsymbol{\Omega}_c) = \mathbf{S}^T \mathbf{T}. \quad (4)$$

where M is the mass of the rigid body, \mathbf{I}_B is the inertia matrix in Σ_B (that is, \mathbf{I}_B is a constant matrix), and $\mathbf{S}(t)$ is the rotational matrix which transforms the basis vectors of Σ_A to these of Σ_B at time t (see Appendix A.1). Note that \mathbf{S}^T represents the transpose of \mathbf{S} .

We will need to determine positions and velocities of the Lagrangian points which move together with the body motion. They are determined by the kinematic equations shown in Appendix A.1.

2.3. Force and torque acting on the body

The force acting on the body $\mathbf{F}(t)$ can be calculated by the negative of the sum of the body forces $\mathbf{g}(\mathbf{x}, t)$ on the boundary shell [4]. However, the negative of the sum of the body forces over the boundary shell is equal to the force $\mathbf{F}_{\text{tot}}(t)$ which the boundary shell receive from both the internal and the external fluid:

$$\mathbf{F}_{\text{tot}}(t) = - \int_{\mathbf{x} \in L_\epsilon(t)} \mathbf{g}(\mathbf{x}, t) d\mathbf{x}. \quad (5)$$

In general, $\mathbf{F}_{\text{tot}}(t)$ is not equal to $\mathbf{F}(t)$, because a part of the summation of the body forces is used to move the internal fluid. Hence, in order to calculate $\mathbf{F}(t)$, we must compensate $\mathbf{F}_{\text{tot}}(t)$ with the force $\mathbf{F}_{\text{in}}(t)$ which is used to move the internal fluid [5,6]. The compensation force $\mathbf{F}_{\text{in}}(t)$ is given by the time derivative of the linear momentum of the internal fluid:

$$\mathbf{F}_{\text{in}}(t) = \rho_f \frac{d}{dt} \int_{\mathbf{x} \in \Omega(t)} \mathbf{u}(\mathbf{x}, t) d\mathbf{x}. \quad (6)$$

As a result, the force acting on the body $\mathbf{F}(t)$ from the external fluid is calculated by

$$\mathbf{F}(t) = \mathbf{F}_{\text{tot}}(t) + \mathbf{F}_{\text{in}}(t). \quad (7)$$

Similarly, the torque $\mathbf{T}(t)$ acting on the body is calculated by

$$\mathbf{T}(t) = \mathbf{T}_{\text{tot}}(t) + \mathbf{T}_{\text{in}}(t), \quad (8)$$

$$\mathbf{T}_{\text{tot}}(t) = - \int_{\mathbf{x} \in L_c(t)} [\mathbf{x} - \mathbf{X}_c(t)] \times \mathbf{g}(\mathbf{x}, t) d\mathbf{x}, \quad (9)$$

$$\mathbf{T}_{\text{in}}(t) = \rho_f \frac{d}{dt} \int_{\mathbf{x} \in Q(t)} [\mathbf{x} - \mathbf{X}_c(t)] \times \mathbf{u}(\mathbf{x}, t) d\mathbf{x}. \quad (10)$$

Hereafter, the compensation force $\mathbf{F}_{\text{in}}(t)$ and torque $\mathbf{T}_{\text{in}}(t)$ are called the *internal mass effect*. There are several schemes for computing the internal mass effect, and the schemes will be introduced in Section 3.

3. Numerical method

We use an IB-LBM for solving Eqs. (1) and (2). The motion of the body determined by Eqs. (3) and (4) is computed by the first-order Euler method. At each time step the force and the torque acting on the body are computed by Eqs. (5)–(10). We use non-dimensional variables defined in Appendix B. Note that the same notations as in Section 2 are used for the non-dimensional variables.

3.1. Lattice Boltzmann method

In the LBM, a modeled gas, which is composed of identical particles whose velocities are restricted to a finite set of vectors, is considered [9]. Two-dimensional lattice with nine velocity vectors (D2Q9 model) and three-dimensional lattice with fifteen velocity vectors (D3Q15 model) are used in the present study. The D2Q9 model has the velocity vectors $\mathbf{c}_i = (0, 0), (0, \pm 1), (\pm 1, 0), (\pm 1, \pm 1)$ for $i = 1, 2, \dots, 9$. The D3Q15 model has the velocity vectors $\mathbf{c}_i = (0, 0, 0), (0, 0, \pm 1), (0, \pm 1, 0), (\pm 1, 0, 0), (\pm 1, \pm 1, \pm 1)$ for $i = 1, 2, \dots, 15$. The evolution of the particle distribution function $f_i(\mathbf{x}, t)$ with the velocity \mathbf{c}_i at the point \mathbf{x} and time t is computed by the following equations:

$$f_i(\mathbf{x} + \mathbf{c}_i \Delta x, t + \Delta t) = f_i(\mathbf{x}, t) - \frac{1}{\tau} [f_i(\mathbf{x}, t) - f_i^{\text{eq}}(\mathbf{x}, t)], \quad (11)$$

where Δx is a lattice spacing, Δt is the time step during which the particles travel one lattice spacing, f_i^{eq} is an equilibrium function, and τ is a relaxation time of $O(1)$. In Eq. (11), \mathbf{x} is a nondimensional position normalized by a characteristic length H_0 , t is a nondimensional time normalized by a diffusive time scale $t_0 = H_0/U_0$ where U_0 is a characteristic flow speed, and \mathbf{c}_i is a nondimensional particle velocity normalized by a characteristic particle speed c . In the system where a rigid body moves in fluid, H_0 is the scale of the body, and U_0 is the speed of the body. In addition, we assume that U_0/c is of $O(\Delta x)$. Note that $\Delta t = Sh \Delta x$ where $Sh = H_0/(t_0 c) = U_0/c = O(\Delta x)$ (see Appendix B). The equilibrium distribution function f_i^{eq} of the incompressible model [21] is given by

$$f_i^{\text{eq}} = E_i \left[3p + 3\mathbf{c}_i \cdot \mathbf{u} + \frac{9}{2} (\mathbf{c}_i \cdot \mathbf{u})^2 - \frac{3}{2} \mathbf{u} \cdot \mathbf{u} \right], \quad (12)$$

where $E_1 = 4/9$, $E_2 = \dots = E_5 = 1/9$, and $E_6 = \dots = E_9 = 1/36$ for the D2Q9 model, and $E_1 = 2/9$, $E_2 = \dots = E_7 = 1/9$, and $E_8 = \dots = E_{15} = 1/72$ for the D3Q15 model. The pressure $p(\mathbf{x}, t)$ and the flow velocity $\mathbf{u}(\mathbf{x}, t)$ are calculated by

$$p = \frac{1}{3} \sum_{i=1}^b f_i, \quad (13)$$

$$\mathbf{u} = \sum_{i=1}^b f_i \mathbf{c}_i, \quad (14)$$

where $b = 9$ for the D2Q9 model, and $b = 15$ for the D3Q15 model.

It is found that the asymptotic expansions of \mathbf{u} and p with respect to Δx can be expressed by $\mathbf{u} = (\Delta x) \mathbf{u}^{(1)} + (\Delta x)^2 \mathbf{u}^{(2)} + (\Delta x)^3 \mathbf{u}^{(3)} + \dots$ and $p = 1/3 + (\Delta x)^2 p^{(2)} + (\Delta x)^3 p^{(3)} + (\Delta x)^4 p^{(4)} + \dots$, and $\mathbf{u}^{(1)}$ and $p^{(2)}$ satisfy the continuity Eq. (1) and the Navier–Stokes Eq. (2) for incompressible viscous fluid with the kinematic viscosity ν given by

$$\nu = \frac{1}{3} \left(\tau - \frac{1}{2} \right) \Delta x, \quad (15)$$

while $\mathbf{u}^{(2)}$ and $p^{(3)}$ are zero with appropriate initial and boundary conditions [22,23]. That is, the solutions of Eqs. (11)–(14) give the pressure and the velocities for incompressible viscous fluid flows with relative errors of $O[(\Delta x)^2]$.

When an external body force $\mathbf{g}(\mathbf{x}, t)$ is applied, the evolution Eq. (11) of the particle distribution function $f_i(\mathbf{x}, t)$ can be calculated in a stepwise fashion as follows:

1. $f_i(\mathbf{x}, t)$ is evolved without the body force by

$$f_i^*(\mathbf{x} + \mathbf{c}_i \Delta x, t + \Delta t) = f_i(\mathbf{x}, t) - \frac{1}{\tau} [f_i(\mathbf{x}, t) - f_i^{\text{eq}}(\mathbf{x}, t)]. \quad (16)$$

2. f_i^* is corrected by the body force:

$$f_i(\mathbf{x}, t + \Delta t) = f_i^*(\mathbf{x}, t + \Delta t) + 3\Delta x E_i \mathbf{c}_i \cdot \mathbf{g}(\mathbf{x}, t + \Delta t). \quad (17)$$

3.2. Immersed boundary method

In the IBM, it is assumed that an incompressible viscous fluid is filled in both inside and outside of the boundary. Then, the body forces are applied on lattice points near the boundary in order to enforce the no-slip condition on the boundary. The scheme for determining the body forces is different between variations of the IBM. In this study, we use the Multi Direct Forcing Method (MDFM) proposed by Wang et al. [19].

Supposing that $f_i(\mathbf{x}, t)$, $\mathbf{u}(\mathbf{x}, t)$ and $p(\mathbf{x}, t)$ are known, the temporal $f_i^*(\mathbf{x}, t + \Delta t)$ and $\mathbf{u}_i^*(\mathbf{x}, t + \Delta t)$ can be calculated by Eqs. (16) and (14), respectively. Let $\mathbf{X}_k(t + \Delta t)$ and $\mathbf{U}_k(t + \Delta t)$ ($k = 1, \dots, N$) be the Lagrangian points of the moving boundary and the boundary velocity at the points, respectively. Note that the moving boundary is represented by N points, and the boundary Lagrangian points \mathbf{X}_k generally differ from the Eulerian grid points \mathbf{x} . Then, the temporal velocities $\mathbf{u}_i^*(\mathbf{X}_k, t + \Delta t)$ at the boundary Lagrangian points \mathbf{X}_k are interpolated by

$$\mathbf{u}^*(\mathbf{X}_k, t + \Delta t) = \sum_{\mathbf{x}} \mathbf{u}^*(\mathbf{x}, t + \Delta t) W(\mathbf{x} - \mathbf{X}_k) (\Delta x)^d, \quad (18)$$

where $\sum_{\mathbf{x}}$ describes the summation over all lattice points \mathbf{x} , W is a weighting function proposed by Peskin [24], and d is the dimensionality. The weighting function W is given by

$$W(x, y, z) = \frac{1}{\Delta x} w\left(\frac{x}{\Delta x}\right) \cdot \frac{1}{\Delta x} w\left(\frac{y}{\Delta x}\right) \cdot \frac{1}{\Delta x} w\left(\frac{z}{\Delta x}\right), \quad (19)$$

$$w(r) = \begin{cases} \frac{1}{8} (3 - 2|r| + \sqrt{1 + 4|r| - 4r^2}), & |r| \leq 1 \\ \frac{1}{8} (5 - 2|r| - \sqrt{-7 + 12|r| - 4r^2}), & 1 \leq |r| \leq 2 \\ 0, & \text{otherwise.} \end{cases} \quad (20)$$

It should be noted that Eq. (19) shows that the three-dimensional weighting function is the product of three one-dimensional weighting functions, and the two-dimensional weighting function can be gained as the product of two one-dimensional weighting functions.

The body force $\mathbf{g}(\mathbf{x}, t + \Delta t)$ is determined by the following iterative procedure.

Step 0. Compute the initial value of the body force at the boundary Lagrangian points by

$$\mathbf{g}_0(\mathbf{X}_k, t + \Delta t) = Sh \frac{\mathbf{U}_k - \mathbf{u}^*(\mathbf{X}_k, t + \Delta t)}{\Delta t}, \quad (21)$$

where it is noted that $Sh/\Delta t = 1/\Delta x$ as defined in Section 3.1.

Step 1. Compute the body force at the Eulerian grid points of ℓ th iteration by

$$\mathbf{g}_\ell(\mathbf{x}, t + \Delta t) = \sum_{k=1}^N \mathbf{g}_\ell(\mathbf{X}_k, t + \Delta t) W(\mathbf{x} - \mathbf{X}_k) \Delta V, \quad (22)$$

where the body force is not added to one boundary Lagrangian point but a small volume element whose volume is described as ΔV . In this method, ΔV is taken as $S/N \times \Delta x$ where S is the area of the body surface, and S/N is taken to be approximately equal to $(\Delta x)^{d-1}$.

Step 2. Correct the velocity at the Eulerian grid point by

$$\mathbf{u}_\ell(\mathbf{x}, t + \Delta t) = \mathbf{u}^*(\mathbf{x}, t + \Delta t) + \frac{\Delta t}{Sh} \mathbf{g}_\ell(\mathbf{x}, t + \Delta t). \quad (23)$$

Step 3. Interpolate the velocity at the boundary Lagrangian point with

$$\mathbf{u}_\ell(\mathbf{X}_k, t + \Delta t) = \sum_{\mathbf{x}} \mathbf{u}_\ell(\mathbf{x}, t + \Delta t) W(\mathbf{x} - \mathbf{X}_k) (\Delta x)^d. \quad (24)$$

Step 4. Correct the body force with

$$\begin{aligned} \mathbf{g}_{\ell+1}(\mathbf{X}_k, t + \Delta t) &= \mathbf{g}_\ell(\mathbf{X}_k, t + \Delta t) + Sh \\ &\times \frac{\mathbf{U}_k - \mathbf{u}_\ell(\mathbf{X}_k, t + \Delta t)}{\Delta t}, \end{aligned} \quad (25)$$

and go **Step 1**.

From preliminary computations, we found that $\mathbf{g}_{\ell=5}(\mathbf{x}, t + \Delta t)$ is enough to keep no-slip condition on the boundary points (see Appendix D). Therefore, we iterate the above procedure until $\ell = 5$ in the following computations.

3.3. Body motion

The first-order Euler method is used for the computations of Eqs. (3) and (4) as follows:

$$\mathbf{U}_c(t + \Delta t) = \mathbf{U}_c(t) + \frac{\Delta t}{Sh} M^{-1} [\mathbf{F}_{\text{tot}}(t) + \mathbf{F}_{\text{in}}(t)], \quad (26)$$

$$\begin{aligned} {}^B\Omega_c(t + \Delta t) &= {}^B\Omega_c(t) \\ &+ \frac{\Delta t}{Sh} \mathbf{I}_B^{-1} \left[\mathbf{S}(t)^T (\mathbf{T}_{\text{tot}}(t) + \mathbf{T}_{\text{in}}(t)) - {}^B\Omega_c(t) \times (\mathbf{I}_B {}^B\Omega_c(t)) \right], \end{aligned} \quad (27)$$

where $\mathbf{F}_{\text{tot}}(t)$ and $\mathbf{T}_{\text{tot}}(t)$ given by Eqs. (5) and (9) are calculated as follows:

$$\mathbf{F}_{\text{tot}}(t) = - \sum_{\mathbf{x}} \mathbf{g}(\mathbf{x}, t) (\Delta x)^d, \quad (28)$$

$$\mathbf{T}_{\text{tot}}(t) = - \sum_{\mathbf{x}} (\mathbf{x} - \mathbf{X}_c(t)) \times \mathbf{g}(\mathbf{x}, t) (\Delta x)^d. \quad (29)$$

On the other hand, in order to calculate the internal mass effect $\mathbf{F}_{\text{in}}(t)$ and $\mathbf{T}_{\text{in}}(t)$ given by Eqs. (6) and (10), we introduce the following four schemes (A), (B-1), (B-2), and (C).

(A) No internal mass effect

The internal mass effect is ignored, that is,

$$\mathbf{F}_{\text{in}}(t) \approx \mathbf{0}, \quad \mathbf{T}_{\text{in}}(t) \approx \mathbf{0}. \quad (30)$$

The internal mass effect has usually been ignored since Peskin [1] proposed the IBM. Even in recent work by Liao et al. [25] they ignore the internal mass effect in the simulation of a moving cylinder problem.

(B) Rigid body approximation

The simple way to approximate Eqs. (6) and (10) is to assume the rigid body motion inside $\Omega(t)$ [6] as follows:

$$\mathbf{F}_{\text{in}}(t) = \frac{\rho_f}{\rho_b} M Sh \frac{d\mathbf{U}_c}{dt}, \quad (31)$$

$$\mathbf{T}_{\text{in}}(t) \approx \frac{\rho_f}{\rho_b} \mathbf{S}(t) \left[\mathbf{I}_B Sh \frac{d^B\Omega_c}{dt} + {}^B\Omega_c(t) \times (\mathbf{I}_B {}^B\Omega_c(t)) \right]. \quad (32)$$

It must be noted that the equality is theoretically realized in Eq. (31), since the linear momentum of the internal mass is exactly equal to that of the rigid body in spite of actual internal flows (see Appendix C). On the other hand, the equality is not satisfied in the approximation for the angular momentum (32). There are two ways to discretize $d\mathbf{U}_c/dt$ and $d^B\Omega_c/dt$ in time as follows.

(B-1) Uhlmann's rigid body approximation [6]

The time derivative is approximated by the change between two successive time t and $t + \Delta t$. That is, setting $\mathbf{F}_{\text{in}}(t) = \mathbf{T}_{\text{in}}(t) = \mathbf{0}$, we replace M and \mathbf{I}_B in Eqs. (26) and (27) with M^{eff} and $\mathbf{I}_B^{\text{eff}}$ defined by

$$M^{\text{eff}} = \left(1 - \frac{\rho_f}{\rho_b} \right) M, \quad (33)$$

$$\mathbf{I}_B^{\text{eff}} = \left(1 - \frac{\rho_f}{\rho_b} \right) \mathbf{I}_B. \quad (34)$$

In this approximation, the internal mass effect is calculated implicitly. It should be noted that this approximation has a limitation of the density ratio $\gamma = \rho_b/\rho_f$ for stable computations, since $\gamma = 1$ is a singular value for the equations of the body motion. It seems that the critical value of the limitation is dependent on the overall numerical scheme and the computational problems. According to Uhlmann[6], in the case of a solid particle accelerating from rest due to gravity, the limitation of the density ratio is $\gamma \gtrsim 1.05$ for circular disks and $\gamma \gtrsim 1.2$ for spherical particles.

(B-2) Feng's rigid body approximation [7]

The time derivative is approximated by the change between two successive time $t - \Delta t$ and t :

$$\mathbf{F}_{\text{in}}(t) \approx \frac{\rho_f}{\rho_b} M Sh \frac{\mathbf{U}_c(t) - \mathbf{U}_c(t - \Delta t)}{\Delta t}, \quad (35)$$

$$\mathbf{T}_{\text{in}}(t) \approx \frac{\rho_f}{\rho_b} \mathbf{S}(t) \left[\mathbf{I}_B Sh \frac{{}^B\Omega_c(t) - {}^B\Omega_c(t - \Delta t)}{\Delta t} + {}^B\Omega_c(t) \times (\mathbf{I}_B {}^B\Omega_c(t)) \right]. \quad (36)$$

where at $t=0$ we assume that $\mathbf{U}_c(-\Delta t) = \mathbf{U}_c(0)$ and ${}^B\Omega_c(-\Delta t) = {}^B\Omega_c(0)$. In contrast to (B-1), this approximation is an explicit method and has no limitation of the density ratio for stable computations.

(C) Lagrangian points approximation

The most straightforward approximations of Eqs. (6) and (10) are the sums of linear and angular momentums of the internal mass over internal Lagrangian points $\mathbf{X}_{\text{in}}(t)$ which move together with the body motion. It should be noted that velocities $\mathbf{u}(\mathbf{X}_{\text{in}}, t)$ on internal Lagrangian points $\mathbf{X}_{\text{in}}(t)$ must be interpolated from neighbor lattice points. The interpolation can be implemented by

$$\mathbf{u}(\mathbf{X}_{\text{in}}, t) = \sum_{\mathbf{x}} \mathbf{u}(\mathbf{x}, t) W(\mathbf{x} - \mathbf{X}_{\text{in}}(t)) (\Delta x)^d. \quad (37)$$

The linear and angular momentums $\mathbf{P}_{\text{in}}(t)$ and $\mathbf{L}_{\text{in}}(t)$ of the internal mass at time t are calculated by

$$\mathbf{P}_{\text{in}}(t) = \sum_{\text{all } \mathbf{X}_{\text{in}}(t)} \mathbf{u}(\mathbf{X}_{\text{in}}, t) \Delta V_{\text{in}}, \quad (38)$$

$$\mathbf{L}_{\text{in}}(t) = \sum_{\text{all } \mathbf{X}_{\text{in}}(t)} [\mathbf{X}_{\text{in}}(t) - \mathbf{X}_{\text{c}}(t)] \times \mathbf{u}(\mathbf{X}_{\text{in}}, t) \Delta V_{\text{in}}, \quad (39)$$

where ΔV_{in} is the volume element of internal Lagrangian points. In the present work, we arrange initial internal Lagrangian points $\mathbf{X}_{\text{in}}(0)$ in lattice points with the width of Δx , and, therefore, we take $\Delta V_{\text{in}} = (\Delta x)^d$. We have confirmed that this arrangement of internal Lagrangian points gives sufficiently accurate results and finer arrangements give almost the same results. The time derivative in $\mathbf{F}_{\text{in}}(t)$ and $\mathbf{T}_{\text{in}}(t)$ is approximated by the change between two successive time $t - \Delta t$ and t as below:

$$\begin{aligned} \mathbf{F}_{\text{in}}(t) &\approx Sh \frac{\mathbf{P}_{\text{in}}(t) - \mathbf{P}_{\text{in}}(t - \Delta t)}{\Delta t}, \\ \mathbf{T}_{\text{in}}(t) &\approx Sh \frac{\mathbf{L}_{\text{in}}(t) - \mathbf{L}_{\text{in}}(t - \Delta t)}{\Delta t}, \end{aligned} \quad (40)$$

where at $t = 0$ we assume that $\mathbf{P}_{\text{in}}(-\Delta t) = \mathbf{P}_{\text{in}}(0)$ and $\mathbf{L}_{\text{in}}(-\Delta t) = \mathbf{L}_{\text{in}}(0)$.

Uhlmann [6] also evaluated \mathbf{P}_{in} and \mathbf{L}_{in} as a sum over internal Eulerian grid points (not over internal Lagrangian points). His method is very easy in the case of a simple shaped body, but it has a computational complexity in the case of a complex shaped body, since we need to search the Eulerian grid points inside the body every time step. On the other hand, the Lagrangian points approximation is a simple algorithm independent of the shape of the body.

The positions and the velocities of boundary Lagrangian points, \mathbf{X}_k and \mathbf{U}_k , are determined from \mathbf{U}_c and ${}^B\mathbf{\Omega}_c$. The determination of \mathbf{X}_k and \mathbf{U}_k is shown in Appendix A.2. Internal Lagrangian points \mathbf{X}_{in} are also determined in the same way as \mathbf{X}_k .

3.4. Algorithm of computation

The algorithm of computation by the present numerical method is summarized as below.

1. Suppose the initial value of $f_i(\mathbf{x}, 0)$, and $\mathbf{g}(\mathbf{x}, 0)$, and compute $\mathbf{u}(\mathbf{x}, 0)$ and $p(\mathbf{x}, 0)$ by Eqs. (13) and (14). Also, assign $\mathbf{X}_c(0)$, $\mathbf{S}(0)$, $\mathbf{U}_c(0)$ and ${}^B\mathbf{\Omega}_c(0)$.
2. Compute $\mathbf{F}_{\text{tot}}(t)$ and $\mathbf{T}_{\text{tot}}(t)$ by Eqs. (28) and (29).
3. Compute $\mathbf{F}_{\text{in}}(t)$ and $\mathbf{T}_{\text{in}}(t)$ in each schemes (A), (B-1), (B-2), and (C) as below:
 - (A) Set $\mathbf{F}_{\text{in}}(t) = \mathbf{T}_{\text{in}}(t) = \mathbf{0}$.
 - (B-1) Set $\mathbf{F}_{\text{in}}(t) = \mathbf{T}_{\text{in}}(t) = \mathbf{0}$, and replace M and \mathbf{I}_B in Eqs. (26) and (27) with M^{eff} and \mathbf{I}^{eff} defined by Eqs. (33) and (34).
 - (B-2) Compute by Eqs. (35) and (36).
 - (C) Compute by Eqs. (37)–(40).
4. Compute $\mathbf{U}_c(t + \Delta t)$ and ${}^B\mathbf{\Omega}_c(t + \Delta t)$ by Eqs. (26) and (27).
5. Compute $\mathbf{X}_k(t + \Delta t)$ and $\mathbf{S}(t + \Delta t)$ by Eqs. (A.1), (A.6), and (A.7). Then, determine $\mathbf{X}_k(t + \Delta t)$ and $\mathbf{U}_k(t + \Delta t)$ by Eqs. (A.8) and (A.9).
6. Compute $f_i^*(\mathbf{x}, t + \Delta t)$ by Eq. (16) and $\mathbf{u}^*(\mathbf{x}, t + \Delta t)$ by Eq. (14). Then, compute $\mathbf{u}^*(\mathbf{X}_k, t + \Delta t)$ by Eq. (18).
7. Compute $\mathbf{g}^*(\mathbf{x}, t + \Delta t)$ by Eqs. (21)–(25).
8. Compute $f_i(\mathbf{x}, t + \Delta t)$ by Eq. (17), and $\mathbf{u}(\mathbf{x}, t + \Delta t)$ and $p(\mathbf{x}, t + \Delta t)$ by Eqs. (13) and (14).
9. Advance one time step and return to 1.

4. Numerical results and discussions

In this section, we investigate the internal mass effect by simulating four unsteady moving boundary problems at the Reynolds

numbers in the range of about 1–100. We compare the four schemes (A), (B-1), (B-2), and (C) described in Section 3.3.

4.1. Translationally oscillating circular cylinder in a stationary fluid

First, we consider an oscillating circular cylinder in a stationary fluid. This problem was studied both experimentally and numerically by Dütsch et al. [26], and has been reported numerically in many studies [8,25,27,28]. The diameter of the cylinder is D , and the width and the height of the computational domain are $55D$ and $35D$, respectively. The cylinder placed at the center of the domain oscillates with the following speed:

$$U_c(t) = -U_{\text{max}} \cos\left(\frac{2\pi}{T}t\right), \quad (41)$$

$$V_c(t) = 0, \quad (42)$$

where $U_c(t)$ and $V_c(t)$ are the velocity components in the x - and y -directions of the cylinder, U_{max} is the amplitude of the velocity, and T is the period. In the simulation, the diameter of the circular cylinder is $D = 50\Delta x$, the number of boundary Lagrangian points along the cylinder surface is $N = 204$, and the number of internal Lagrangian points used in (C) is 1941. The Neumann boundary condition is used at the outer boundary of the domain, i.e., $\mathbf{n} \cdot \nabla f_i = 0$ (\mathbf{n} is the unit vector normal to the boundary). The governing parameters of the system are the Reynolds number $Re = U_{\text{max}}D/\nu$ and the Keulegan–Carpenter number $KC = U_{\text{max}}T/(Sh D)$. It is noted that Re and KC are defined by the nondimensional variables as shown in Appendix B, and by using the spacial amplitude of the oscillation A_m , we can write $KC = 2\pi A_m/D$. It should be noted that since the motion of the circular cylinder is determined in advance and independent of the force acting on the cylinder, the flow field induced by the motion of the cylinder is independent of the schemes (A), (B), and (C) for evaluating $\mathbf{F}_{\text{in}}(t)$.

We calculate three cases for $Re = 100$, 10, and 1 with $KC = 5$. The parameters used in each computation are shown in Table 1. At first, we show the results for the case of $Re = 100$ and $KC = 5$ and compare the results with those by Dütsch et al. [26]. Fig. 2 shows the velocity profiles at four different x locations ($x = -0.6D, 0.0D, 0.6D$, and $1.2D$) for three different phase angles (a) $\phi = 180^\circ$, (b) $\phi = 210^\circ$, and (c) $\phi = 330^\circ$ where $\phi = t/T \times 360^\circ$. It is seen that the present results have good agreements with the experimental data. Fig. 3 shows the time variation of the drag coefficient $C_D = 2F_x/(U_{\text{max}}^2 D)$ where F_x is the force acting on the body in x direction and is calculated by using Eq. (7). It should be noted that since the results by Dütsch et al. [26] are for periods after initial transient flows, we cut off the transients for the first period ($0 \leq t/T < 1$) of our results. Hence, the data in Fig. 3 begin with the second period. In this problem, when we calculate $\mathbf{F}_{\text{in}}(t)$ by using the rigid body approximation (B), we can directly calculate the time derivative in Eq. (31) without discretizing in time. Therefore, there is no difference between (B-1) and (B-2). It is seen from Fig. 3 that the results with (B) and (C) quantitatively agree with the numerical results by Dütsch et al. On the other hand, the result with (A) is quite different from the numerical results by Dütsch et al. These results clearly indicates that the internal mass effect $\mathbf{F}_{\text{in}}(t)$ is significant for evaluating the force acting on the body $\mathbf{F}(t)$. Fig. 4 shows the velocity vectors inside the body observed from the system fixed on the circular cylinder. We can see from Figs. 3 and 4 that the drag coefficients given by (B) and (C) are almost the same, although the internal flows are far from the rigid body motion and

Table 1
The parameters used in simulations of Section 4.1.

	Re	KC	U_{max}	τ
Case 1.1	100	5	0.03	0.5450
Case 1.2	10	5	0.03	0.9500
Case 1.3	1	5	0.003	0.9500

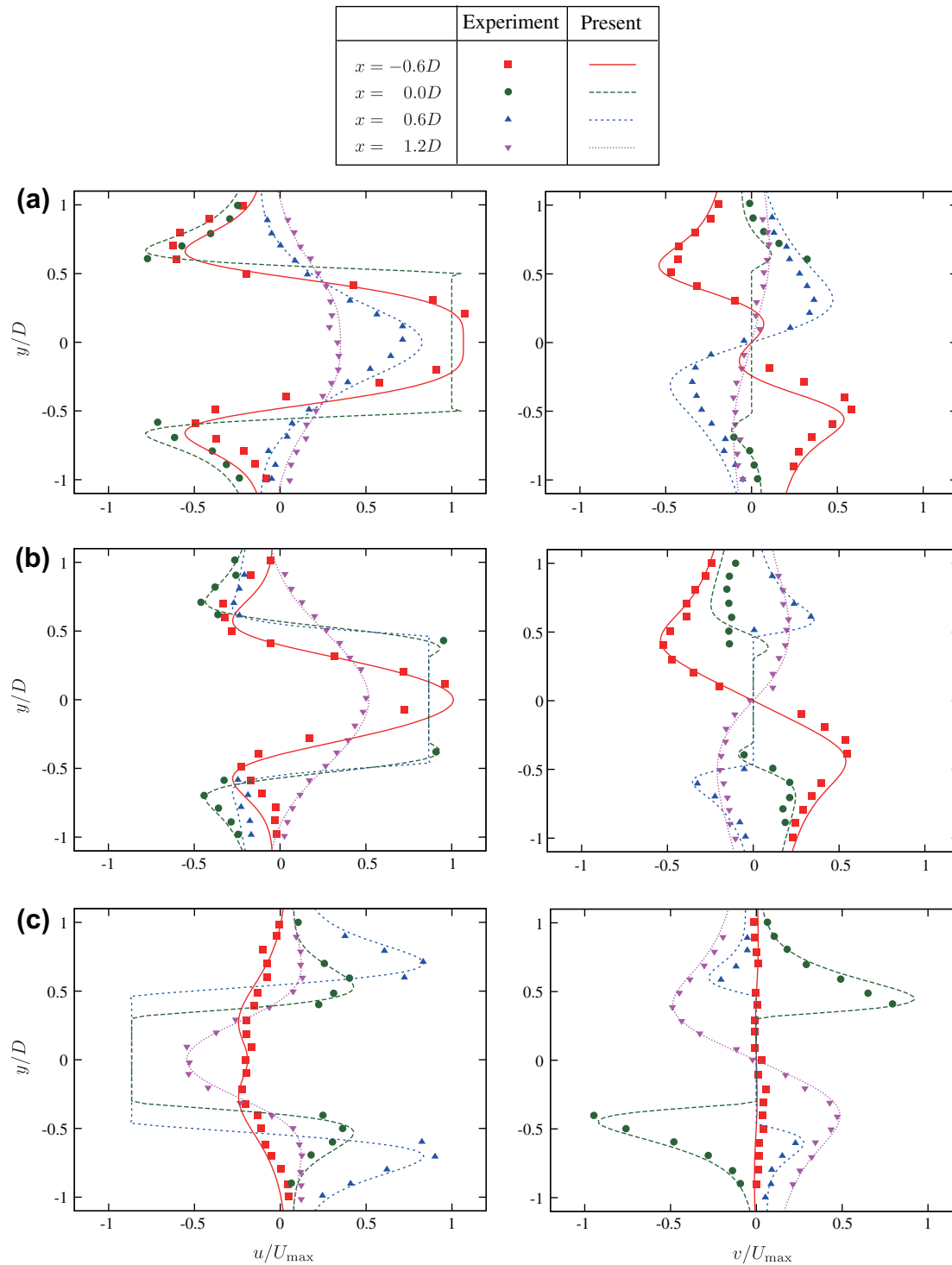


Fig. 2. Velocity profiles for three different phase angles (a) $\phi = 180^\circ$, (b) $\phi = 210^\circ$, and (c) $\phi = 330^\circ$ for $Re = 100$ and $KC = 5$. Lines are the present numerical results, and symbols are the experimental results by Dütsch et al. [26].

the flow patterns are time-dependent. This result is consistent with the fact that the linear momentum of the internal mass is exactly equal to that of the rigid body in spite of actual internal flows (see Appendix C).

Next, we show the results for the cases for $Re = 10$ and 1 with $KC = 5$ in Fig. 5 in order to investigate the effect of the Reynolds number on the internal mass effect $\mathbf{F}_{in}(t)$. It is found from Fig. 5 that the results with (B) and (C) are almost the same, and the difference between the result with (A) and the results with (B) and (C)

decreases as the Reynolds number becomes smaller. The internal mass effect is fairly small at $Re = 1$.

4.2. Rotationally oscillating circular cylinder in a stationary fluid

Secondly, we consider a rotationally oscillating circular cylinder in a stationary fluid. The diameter of the cylinder is D , and the width and the height of the computational domain are both $30D$.

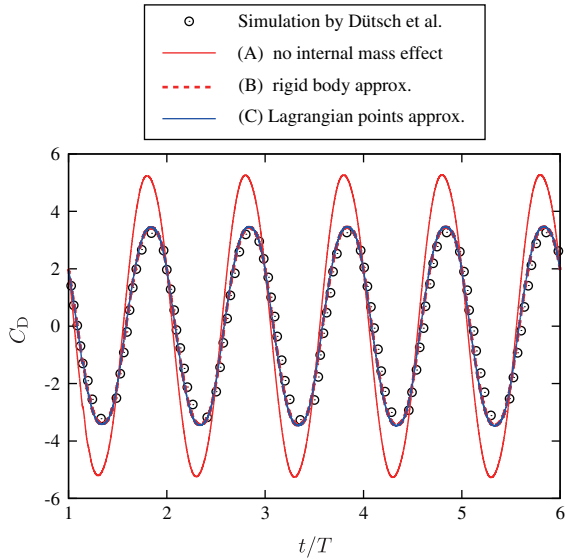


Fig. 3. Time variation of the drag coefficient of a translationally oscillating circular cylinder for $Re = 100$ and $KC = 5$. The results with (A), (B), and (C) are compared with the numerical results by Dütsch et al. [26].

The cylinder placed at the center of the domain rotationally oscillates with the following angular speed:

$$\Omega_c(t) = \Omega_{\max} \sin\left(\frac{2\pi}{T}t\right), \quad (43)$$

where $\Omega_c(t)$ is the angular velocity of the cylinder, Ω_{\max} is the amplitude of the angular velocity, and T is the period. The exact solution of the Navier–Stokes equations for this problem [29] is given by

$$u_\theta(r, t) = \Im\left[\frac{D}{2}\Omega_{\max}\frac{H_1^{(1)}(\beta r)}{H_1^{(1)}(\beta D/2)}\exp\left(i\frac{2\pi}{T}t\right)\right], \quad (44)$$

where u_θ is the azimuthal flow velocity, r is the distance from the center of the cylinder, $\Im[Z]$ means the imaginary part of a complex number Z , $H_1^{(1)}$ is the Hankel function of the first kind of order one, i is the imaginary unit, and $\beta = (-1 + i)\sqrt{\pi Sh/(vT)}$. The torque T_z acting on the circular cylinder is given by

$$T_z(t) = \frac{\pi v D^2}{2} \Im\left[\left(\beta \frac{D}{2} \frac{H_0^{(1)}(\beta D/2)}{H_1^{(1)}(\beta D/2)} - 2\right)\Omega_{\max} \exp\left(i\frac{2\pi}{T}t\right)\right], \quad (45)$$

where $H_0^{(1)}$ is the Hankel function of the first kind of order zero. In the simulation, the diameter of the circular cylinder is $D = 50\Delta x$, the number of boundary Lagrangian points along the cylinder surface is $N = 204$, and the number of internal Lagrangian points used in (C) is 1941. The same condition as Section 4.1 is used at the outer boundary of the domain. The governing parameters of the system are the rotational Reynolds number $Re_r = U_{\max}D/\nu$ where $U_{\max} = \Omega_{\max}D/2$, and the angular amplitude $\Delta\theta = T\Omega_{\max}/(2\pi Sh)$. It is noted that Re_r and $\Delta\theta$ are defined by the nondimensional variables as shown in Appendix B.

We calculate three cases for $Re_r = 100$, 10, and 1 with $\Delta\theta = \pi/4$. The parameters used in each computation are shown in Table 2. It should be noted that the IBM has a problem that the effective radius of the circular cylinder is slightly larger than the input radius [5,7,30], and the effective radius becomes large as Re increases in the simulation of moving sphere [5]. In our numerical tests the discrepancy is distinct especially in the torque acting on the body for high Reynolds numbers. Therefore, in the case of $Re_r = 100$, we distribute the boundary points on the circle whose radius r_{input} is slightly smaller than that of the circular cylinder, namely, $r_{\text{input}} = D/2 - 0.8\Delta x$.

At first, we show the results for the case of $Re_r = 100$ and $\Delta\theta = \pi/4$ and compare the results with the exact solution. Fig. 6a shows the time variation of the azimuthal velocity u_θ at $r = 0.6D$. It should be noted that since the exact solution is for a steady-state oscillation of the circular cylinder and independent of initial conditions, we cut off the transients for the first period ($0 \leq t/T < 1$) of our results. Hence, the data in Fig. 6 begin with the second period. It is seen that the present results have good agreements with the exact solution. The time variation of the torque coefficient $C_T = 2T_z/(U_{\max}^2 D^2)$ is shown in Fig. 6b. In this figure, we show the results of (B) without distinguishing (B-1) and (B-2) for the same reason as the previous problem. We can see that the result with (A) is significantly different from the exact solution, and the result with (B) has a major phase shifting from the exact solution. On the other hand, it can be seen that the result with (C) has a good agreement with the exact solution. These results indicate that the internal mass effect $T_{\text{in}}(t)$ is significant for evaluating the torque acting on the body $T(t)$, and $T_{\text{in}}(t)$ given by (B) has a major error in the case where the angular motion is distinct.

Next, we show the results for the cases of $Re_r = 10$ and 1 with $\Delta\theta = \pi/4$ in Fig. 7 in order to investigate the effect of the Reynolds number on the internal mass effect $T_{\text{in}}(t)$. It is found from Fig. 7 that the difference between the result with (A) and the exact solution decreases as the Reynolds number becomes smaller, and the internal mass effect is negligibly small at $Re_r = 1$. In addition, we can see that as the Reynolds number becomes smaller the

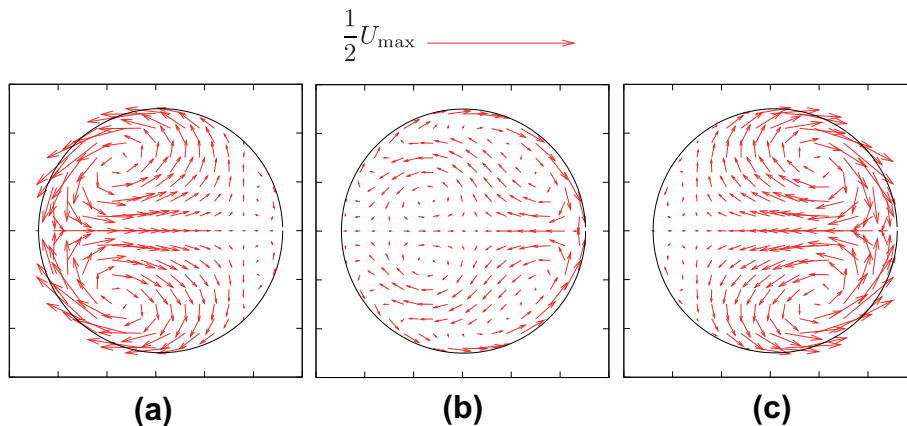


Fig. 4. The internal flows observed from the system fixed on a translationally oscillating circular cylinder for $Re = 100$ and $KC = 5$ for three different phase angles (a) $\phi = 0^\circ$, (b) $\phi = 90^\circ$, and (c) $\phi = 180^\circ$. The velocity vectors are drawn at every 3 lattice points.

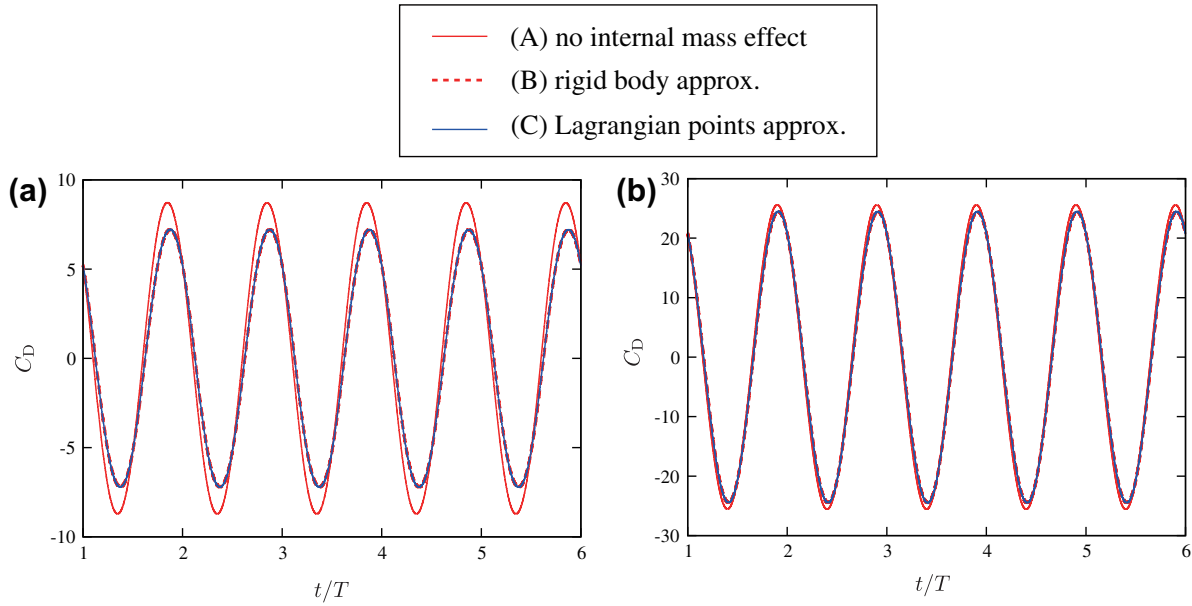


Fig. 5. Time variation of the drag coefficient of a translationally oscillating circular cylinder for (a) $Re = 10$ and $KC = 5$ and (b) $Re = 1$ and $KC = 5$. The results with (A), (B), and (C) are compared each other.

Table 2

The parameters used in simulations of Section 4.2.

	Re_r	$\Delta\theta$	U_{max}	τ
Case 2.1	100	$\pi/4$	0.03	0.5450
Case 2.2	10	$\pi/4$	0.03	0.9500
Case 2.3	1	$\pi/4$	0.003	0.9500

difference between the results with (B) and (C) also decreases and is fairly small at $Re_r = 10$.

4.3. The sedimentation of an elliptical cylinder

Thirdly, we consider an elliptical cylinder falling under gravity in a closed narrow domain filled with fluid. The computational

condition and the coordinate system are shown in Fig. 8. The major and minor axes of the elliptical cylinder are a and b , respectively. The width of the domain is H and the height of the domain is $17.5H$. The major axis is $a = H/4$ and the minor axis is $b = H/8$. The gravity acceleration is α_g . Letting the density ratio of the elliptical cylinder to the fluid be $\gamma = \rho_b/\rho_f$, the mass and the inertia moment of the elliptical cylinder are $M = \gamma(\pi ab/4)$ and $I_B = M(a^2 + b^2)/16$, respectively. The net gravitational force is $F_g = (1 - 1/\gamma)M\alpha_g$, and it is added to $F_{tot}(t)$ in the right hand side of Eq. (26). In the simulation, the domain is divided into the lattice of $200\Delta x \times 3500\Delta x$. The number of boundary Lagrangian points is $N = 154$ and the number of internal Lagrangian points used in (C) is 973. The elliptical cylinder starts its motion at the initial position of $(x_c, y_c) = (0, 0.5H)$ with the initial angle $\theta = 45^\circ$. The bounce back

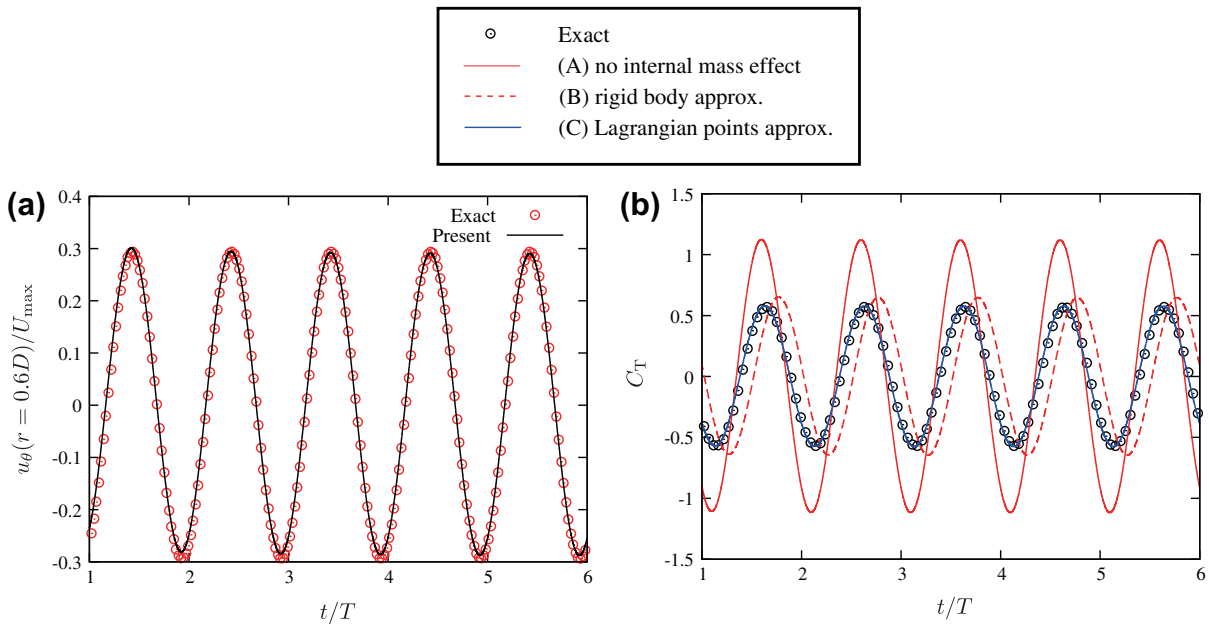


Fig. 6. Time variation of (a) the azimuthal velocity u_θ at $r = 0.6D$ and (b) the torque coefficient for $Re_r = 100$ and $\Delta\theta = \pi/4$ obtained by the simulations of the flow around a rotationally oscillating circular cylinder.

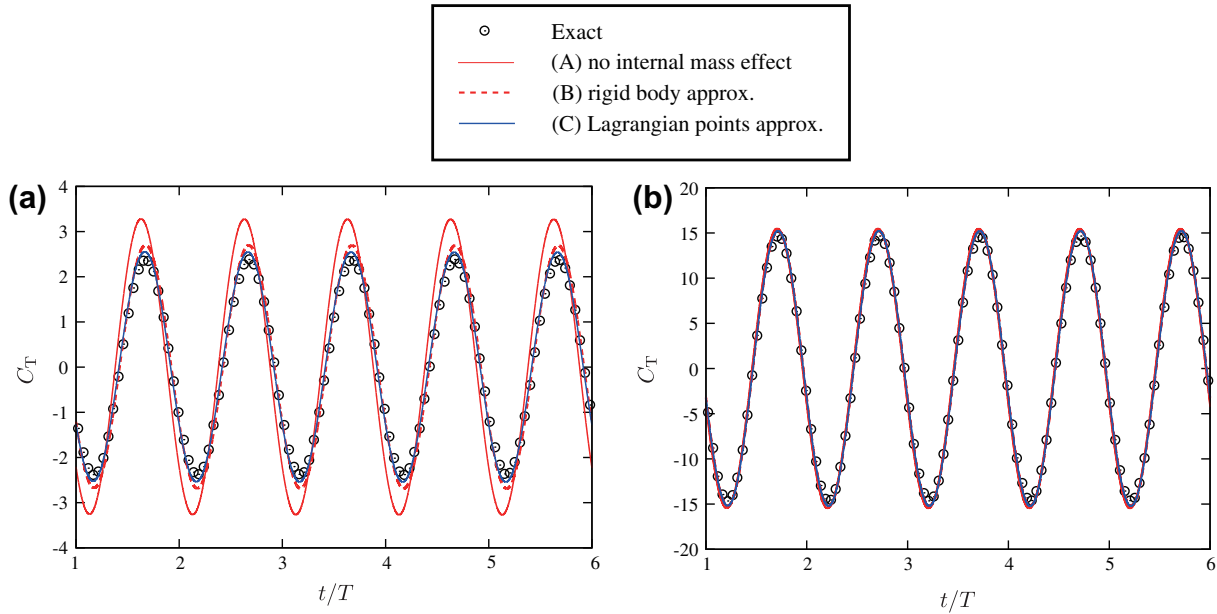


Fig. 7. Time variation of the torque coefficient of a rotationally oscillating circular cylinder for (a) $Re_\tau = 10$ and $\Delta\theta = \pi/4$ and (b) $Re_\tau = 1$ and $\Delta\theta = \pi/4$.

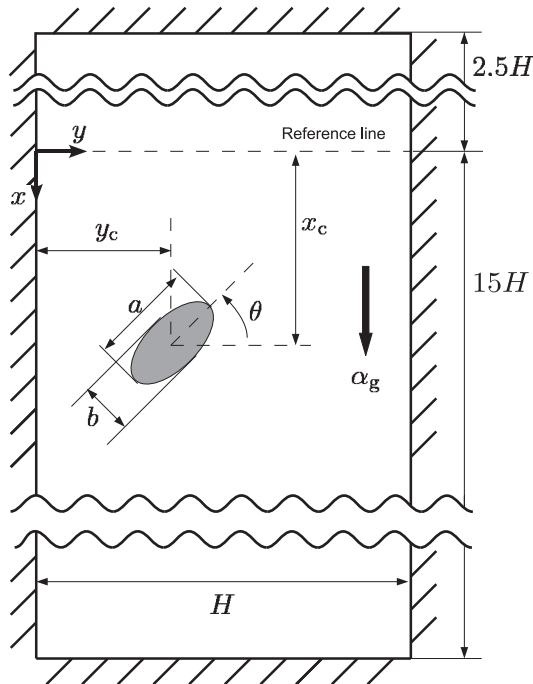


Fig. 8. The domain of computation for an elliptical cylinder falling in a closed narrow domain. The elliptical cylinder is driven by a constant gravity acceleration α_g . The coordinate x is taken in the direction of the gravity and y is in the width of the channel. θ is the cylinder's angle of inclination with respect to the y axis.

condition [9] is used for the outer boundary of the domain. The governing parameters of the system are the density ratio of the elliptical cylinder to the fluid γ and the Reynolds number $Re = u_t a / \nu$, where u_t is the terminal velocity of the elliptical cylinder in the x -direction. It is noted that u_t is obtained by calculations with given τ , α_g , and γ . In the cases where the final state of the motion of the cylinder is of an oscillating nature, the terminal velocity u_t is calculated as the mean value. We calculate three cases as shown in Table 3.

Table 3

The parameters used and obtained in simulations of Section 4.3. The values in parentheses in the columns of u_t and Re are the results with (A), because the calculated motion of the cylinder obtained with (A) in Case 2.1 is significantly different from those with (B-1), (B-2), and (C).

	γ	τ	$\alpha_g \Delta x$	u_t	Re
Case 3.1	1.5	0.6364	1.620×10^{-4}	0.0300 (0.0314)	32.9 (34.5)
Case 3.2	1.1	0.6364	1.620×10^{-4}	0.0115	12.6
Case 3.3	1.01	0.6364	1.620×10^{-4}	0.00175	1.92

Fig. 9 shows the flow field around the elliptical cylinder during falling for the case of $\gamma = 1.5$ and $Re = 32.9$. It can be seen that the elliptical cylinder is horizontally oscillating and the vortices appear behind the elliptical cylinder. Fig. 10 shows the trajectory and the orientation of the elliptical cylinder. Note that the results with (B-1), (B-2), and (C) overlap each other, and thus we cannot distinguish them in the figure. On the other hand, the result with (A) is quite different from the other results with (B-1), (B-2), and (C). That is, the internal mass effect is significant for the body motion, and the three schemes (B-1), (B-2), and (C), which take account of the internal mass effect, give almost the same results. It is noted that the difference among (B-1), (B-2), and (C) is negligible although the angular motion of the elliptical cylinder is distinct. This is because the rotational Reynolds number $Re_r = a^2 \max \{ \|\mathbf{B}\Omega_c\| \} / (2\nu)$ is equal to 9.64, and thus the discrepancy is fairly small as shown in Fig. 7a. Table 4 shows the computation time per one time step, the proportion of the computing time for IBM, LBM and other parts (including the calculations of \mathbf{F}_{in} and \mathbf{T}_{in}) to the total computing time, and the total time steps required until the elliptical cylinder reaches the bottom of the domain. These simulations were performed on a single core of a Core i7 (2.7 GHz).

Next, in order to compare the present result with the numerical result of FEM by Xia et al. [15], we show the results for the case of $\gamma = 1.1$ and $Re = 12.6$ in Fig. 11 where the numerical result of FEM by Xia et al. [15] are also shown. Since the density ratio γ is close to unity, the computation with (B-1) was blown up. It can be seen that the results with (B-2) and (C) have good agreements with the result by FEM, while the result with (A) is slightly different from the other results. From the above results, we see that (B-2) and

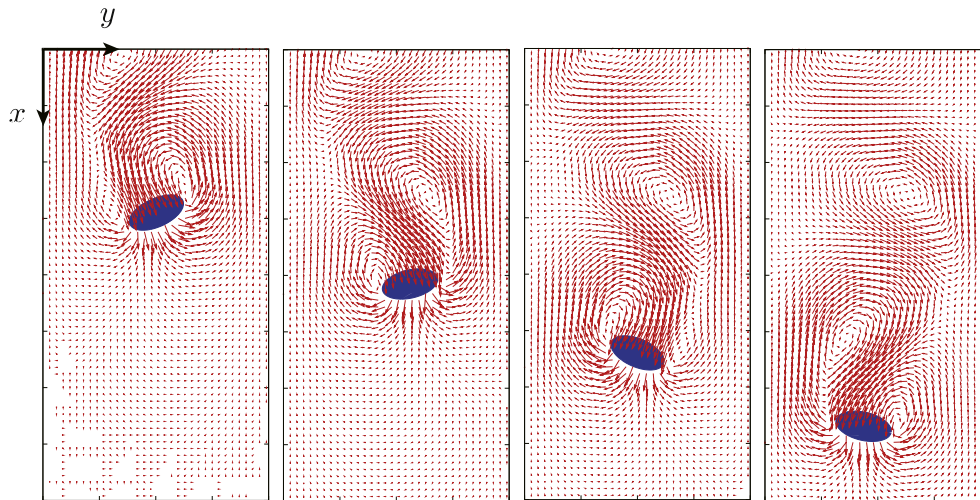


Fig. 9. Flow fields during oscillatory sedimentation of an elliptical cylinder with $\gamma = 1.5$ at $Re = 32.9$.

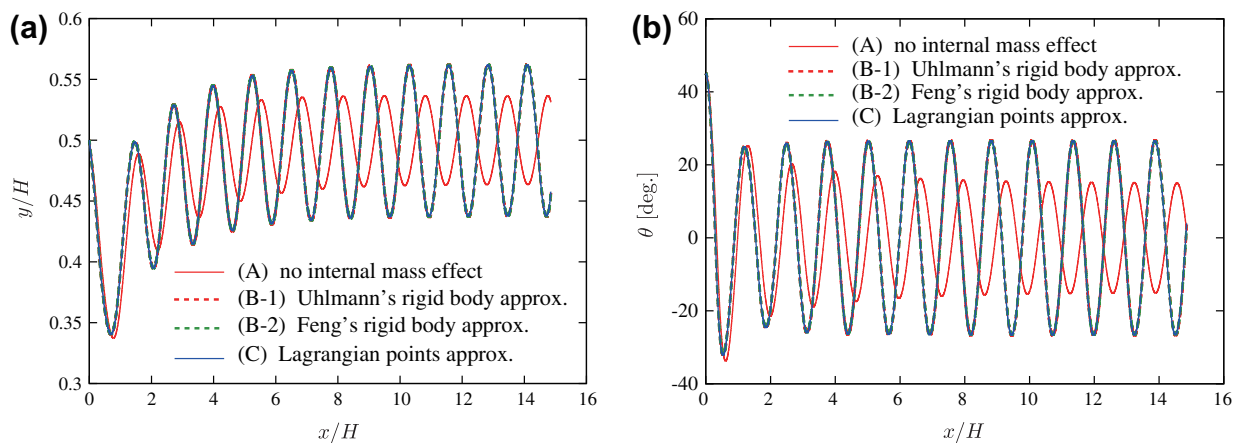


Fig. 10. Trajectory and orientation of an elliptical cylinder with $\gamma = 1.5$ at $Re = 32.9$. (a) Horizontal position of the center of the elliptical cylinder and (b) orientation of the elliptical cylinder.

Table 4

The computation time per one time step, the proportion of the computing time for IBM, LBM and other parts to the total computing time, and the total time steps in the simulations of the sedimentation of an elliptical cylinder with $\gamma = 1.5$ at $Re = 32.9$.

	(A)	(B-1)	(B-2)	(C)
Computation time per one time step (s)	5.69×10^{-2}	5.69×10^{-2}	5.69×10^{-2}	6.65×10^{-2}
Proportion of IBM (%)	28.1	28.2	28.2	24.1
Proportion of LBM (%)	71.8	71.7	71.7	61.3
Proportion of other parts (%)	0.1	0.1	0.1	14.6
Total time steps	96,204	99,600	99,602	99,589

(C) are stable even in the case that the density ratio is close to unity and give reasonable results. In addition, we can see that the internal mass effect is relatively small at $Re = 12.6$ compared with the case at $Re = 32.9$ as shown in Fig. 10. Fig. 12 shows the results for the case of $\gamma = 1.01$ and $Re = 1.92$. In this case, the result with (B-1) was also blown up for the same reason with the previous case. We can see from Fig. 12 that the result with (A) is almost coincident with the results with (B-2) and (C). It is seen that the internal mass effect is fairly small at Re about 1.

4.4. The sedimentation of a sphere

Finally, we consider a sphere falling under gravity in a closed box filled with fluid as shown in Fig. 13. This problem was measured using a PIV system by ten Cate et al. [5]. The experimental

conditions are presented below with dimensional variables. The dimensions of the box are depth \times width \times height = $100 \times 100 \times 160$ mm. The diameter of the sphere is $D_p = 15$ mm and its density is $\rho_b = 1120$ kg/m³. The fluid is initially at rest, and the sphere starts its motion at a height 120 mm from the bottom of the domain due to the gravity acceleration $\alpha_g = 9.8$ m/s². The mass and the inertia moment of the sphere are $M = \rho_b(\pi D_p^3/6)$ and $I_B = MD_p^2/10$, respectively. The inertia matrix of the sphere is given by $I_B = \text{diag}(I_B, I_B, I_B)$. The net gravitational force is $F_g = (1 - \rho_f/\rho_b)M\alpha_g$, and its nondimensional form is added to $\mathbf{F}_{\text{tot}}(t)$ in the right hand side of Eq. (26). In the simulation, the domain is divided into $200 \times 200 \times 320$ lattice grid. Hence, 30 lattice spacings are used for the diameter of the sphere. The number of boundary Lagrangian points is $N = 2840$ and the number of internal Lagrangian points used in (C) is 13997. The bounce back condition is used for

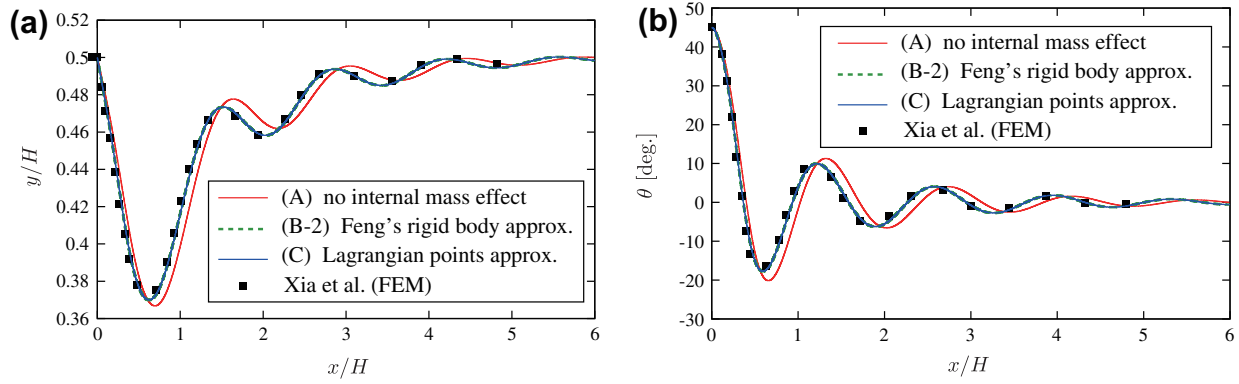


Fig. 11. Trajectory and orientation of an elliptical cylinder with $\gamma = 1.1$ at $Re = 12.6$. (a) Horizontal position of the center of the elliptical cylinder and (b) orientation of the elliptical cylinder.

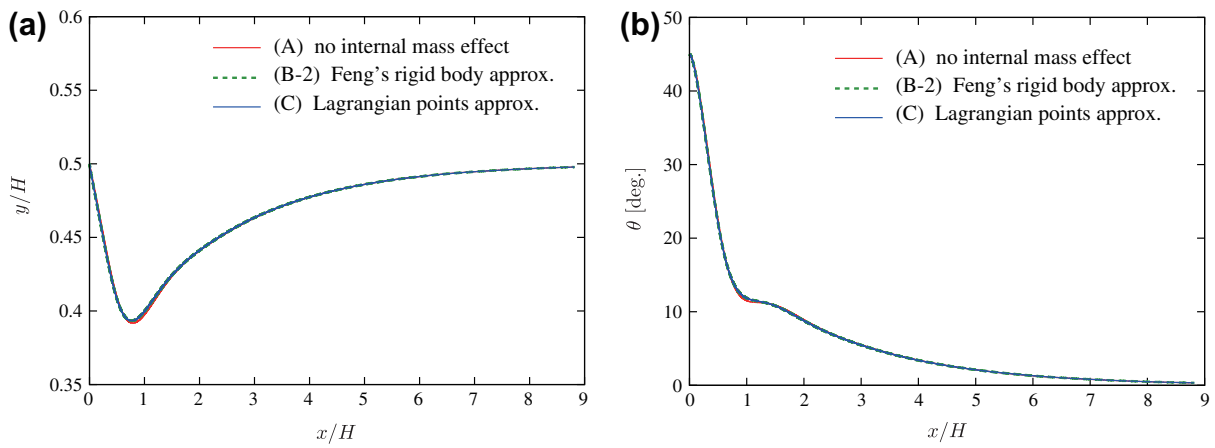


Fig. 12. Trajectory and orientation of an elliptical cylinder with $\gamma = 1.01$ at $Re = 1.92$. (a) Horizontal position of the center of the elliptical cylinder and (b) orientation of the elliptical cylinder.

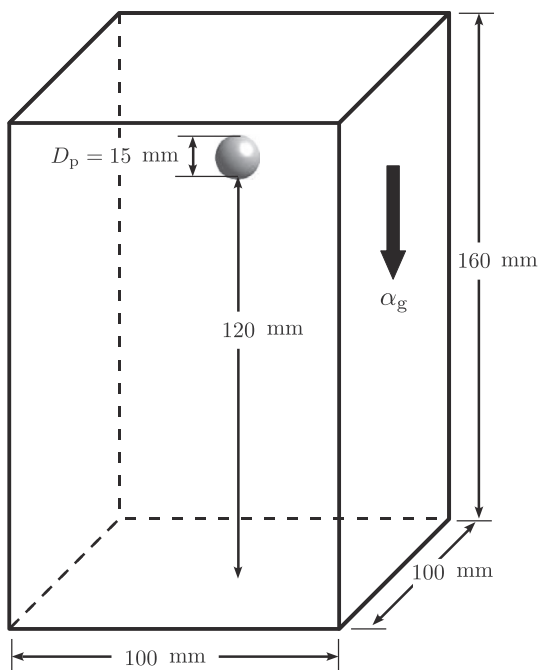


Fig. 13. The domain of computation for a sphere falling in a closed box. The sphere is driven by a constant gravity acceleration α_g .

enforcing the no-slip condition on the outer boundary of the box. In the experiments by ten Cate et al. [5], a liquid free surface exists at the top of the domain. In spite of this, we use the no-slip condition at the top of the domain instead of the free surface condition. This is because it is difficult to achieve the free surface condition, and the influence of the mismatch of the boundary conditions on the top of the domain is considered to be small. In addition, several researchers also use the no-slip condition and obtain good results in the same problem [7,13,25]. We use no repulsive force when the gap L between the sphere and the bottom of the domain is close to zero, while Feng et al. [13,7] employed in their simulations. So, we stop our simulations when L is less than 2 lattice spacings. The governing parameters of the system are the density ratio of the sphere to the fluid $\gamma = \rho_b/\rho_f$ and the Reynolds number $Re = \rho_f u_\infty D_p/\mu$, where u_∞ is the sedimentation velocity of a sphere in an infinite domain [5] and μ is the fluid viscosity.

We calculate four cases as listed in Table 5. The simulated results of the gap L and the falling velocity u are shown in Fig. 14 with the experimental results by ten Cate et al. [5]. Because the density ratios are close to unity in all cases, the results with (B-1) were blown up. It can be seen that the results with (B-2) and (C) coincide with each other and agree reasonably well with the experimental data for all Re , although there is a small discrepancy in the maximum velocity in Fig. 14b. It is thought that the discrepancy is due to the effective radius of the sphere which is slightly larger than the input radius [5,7,30]. However, the effective radius is not discussed further because it is not the principal subject of this

Table 5

Fluid properties in the experiment by ten Cate et al. [5] and the parameters used in simulations of Section 4.4. The gravity acceleration α_g in this table is the nondimensional value defined in Appendix B.

	Re	ρ_f (kg/m ³)	μ ($\times 10^{-3}$ Ns/m ²)	τ	$\alpha_g \Delta x$
Case 4.1	1.5	970	373	1.1000	3.314×10^{-4}
Case 4.2	4.1	965	212	1.1585	1.223×10^{-3}
Case 4.3	11.6	962	113	0.7328	5.344×10^{-4}
Case 4.4	32.2	960	58	0.5839	2.622×10^{-4}

paper. On the other hand, we can see that the results with (A) are slightly different from the experimental data at $Re = 32.2$ and 11.6. Especially, the discrepancy of the velocity in the accelerated phase is distinct. The similar discrepancy is found in numerical results by Liao et al. [25], whose method uses no internal mass effect. In addition, it can be seen that the difference between (A) and the experimental data becomes large as Re increases. These results indicate that the internal mass effect grows as Re increases and becomes distinguishable at Re about 10. This fact is consistent with the results of 2D simulations in Sections 4.1, 4.2, and 4.3.

4.5. Summary of four schemes

At the end of this section, in Table 6 we summarize the ranges of the limitation of Re , Re_r , and $\gamma = \rho_b/\rho_f$ where accurate results can be obtained by the four schemes (A), (B-1), (B-2), and (C). It is noted that our simulations are performed for Re and Re_r in the range of 1–100 and $1.01 \leq \gamma \leq 1.5$. Also, the limitation $\gamma \gtrsim 1.5$ of

Table 6

The ranges of the limitation of Re , Re_r , and $\gamma = \rho_b/\rho_f$ where accurate results can be obtained by the four schemes (A), (B-1), (B-2), and (C). The symbol ' \lesssim ' denotes 'less than or similar to', and ' \gtrsim ' denotes 'greater than or approximately equal to'.

	Re	Re_r	γ
(A)	$\lesssim 1$	$\lesssim 1$	Unlimited
(B-1)	Unlimited	$\lesssim 10$	$\gtrsim 1.5$
(B-2)	Unlimited	$\lesssim 10$	Unlimited
(C)	Unlimited	Unlimited	Unlimited

(B-1) sensitively depends on problems, numerical methods, and mesh sizes of computations. Further investigation for higher Re and Re_r about 1000 and for other values of γ ($\gamma > 1.5$ and $\gamma < 1.01$) is remained in future work.

5. Conclusions

We have investigated the internal mass effect for various Reynolds numbers in the range of about 1–100 through the simulations of a moving body in fluid by using an IB-LBM. As the result, we find that the internal mass effect is fairly small for Reynolds numbers about 1, but grows as Reynolds numbers increases, and the effect becomes distinct for Reynolds numbers over 10. In addition, we compare the rigid body approximations proposed in the literatures with the Lagrangian points approximation proposed in this paper. We find that the rigid body approximation has no error in calculating \mathbf{F}_{in} , but has a major error in calculating \mathbf{T}_{in} in the case where the angular motion of the body is distinct. It is also found that the discrepancy of the rigid body approximation is fairly small in the case for low rotational Reynolds numbers less than 10. It is noted that unlike Uhlmann's rigid body approximation, Feng's rigid body approximation and the Lagrangian points approximation are stable even if the density ratio of the body to the fluid is close to unity.

Appendix A. Kinematics of a rigid body

In this section, we look the kinematics of a rigid body in order to determine positions and velocities of boundary Lagrangian points. In Appendix A.1, we use dimensional variables in the same way as Section 2, while in Appendix A.2 we use nondimensional variables in the same as Section 3.

A.1. Formulation of the kinematic equations

A unit quaternion $\mathbf{Q} = (q_0, q_1, q_2, q_3)^T$ is used to represent \mathbf{S} as below:

$$\mathbf{S} = \begin{bmatrix} q_0^2 - q_1^2 - q_2^2 + q_3^2 & 2(q_1q_2 - q_0q_3) & 2(q_1q_3 + q_0q_2) \\ 2(q_1q_2 + q_0q_3) & q_0^2 - q_3^2 - q_1^2 + q_2^2 & 2(q_2q_3 - q_0q_1) \\ 2(q_1q_3 - q_0q_2) & 2(q_2q_3 + q_0q_1) & q_0^2 - q_1^2 - q_2^2 + q_3^2 \end{bmatrix}, \quad (\text{A.1})$$

where

$$q_0^2 + q_1^2 + q_2^2 + q_3^2 = 1. \quad (\text{A.2})$$

The kinematic equations of the rigid body are as below:

$$\frac{d\mathbf{X}_c}{dt} = \mathbf{U}_c(t), \quad (\text{A.3})$$

$$\frac{d\mathbf{Q}}{dt} = \mathbf{A}(t)\mathbf{Q}(t), \quad (\text{A.4})$$

where $\mathbf{A}(t)$ is a 4×4 matrix which is determined by ${}^B\boldsymbol{\Omega}_c = (\omega_1, \omega_2, \omega_3)^T$ as below:

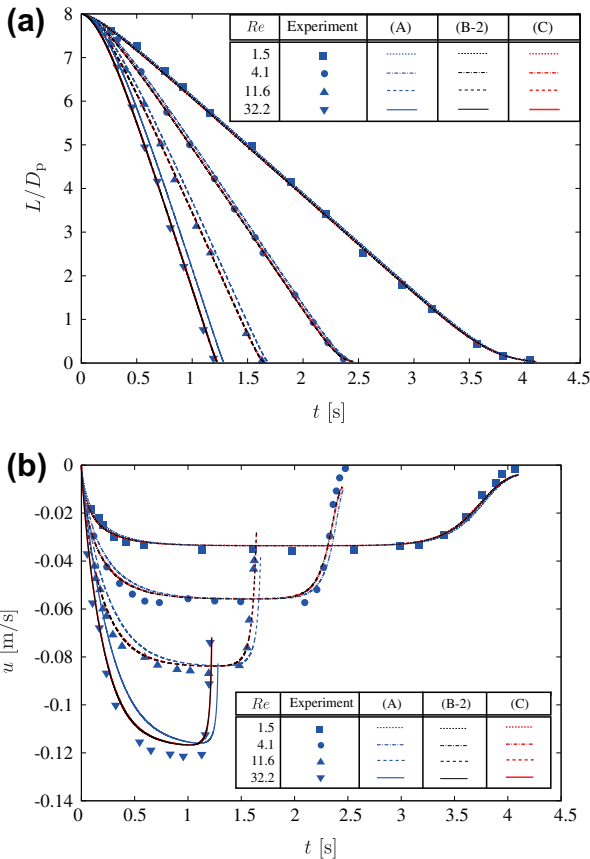


Fig. 14. Comparisons of results with (A), (B-2), and (C) to experimental results by ten Cate et al. [5]: (a) The time variation of the gap L between the sphere and the bottom of the domain and (b) the time variation of the velocity of the sphere u .

$$\mathbf{A} = \frac{1}{2} \begin{bmatrix} 0 & -\omega_1 & -\omega_2 & -\omega_3 \\ \omega_1 & 0 & \omega_3 & -\omega_2 \\ \omega_2 & -\omega_3 & 0 & \omega_1 \\ \omega_3 & \omega_2 & -\omega_1 & 0 \end{bmatrix}. \quad (\text{A.5})$$

A.2. Determination of the position and velocity of a boundary point

In this study, the first-order Euler method is used for the computations of Eq. (A.3) as below:

$$\mathbf{X}_c(t + \Delta t) = \mathbf{X}_c(t) + \frac{\Delta t}{Sh} \mathbf{U}_c(t). \quad (\text{A.6})$$

On the other hand, in order to decrease the error of $\mathbf{Q}(t)$ from the condition (A.2), the second-order modified Euler method is used for the computations of Eq. (A.4) as below:

$$\begin{cases} \tilde{\mathbf{Q}}(t + \Delta t) = \mathbf{Q}(t) + \frac{\Delta t}{Sh} \mathbf{A}(t) \mathbf{Q}(t), \\ \mathbf{Q}(t + \Delta t) = \mathbf{Q}(t) + \frac{\Delta t}{2Sh} [\mathbf{A}(t) \mathbf{Q}(t) + \mathbf{A}(t + \Delta t) \tilde{\mathbf{Q}}(t + \Delta t)]. \end{cases} \quad (\text{A.7})$$

The position \mathbf{X}_k and velocity \mathbf{U}_k of a boundary point are calculated by following equations:

$$\mathbf{X}_k = \mathbf{X}_c + \mathbf{S}^B \mathbf{X}_k, \quad (\text{A.8})$$

$$\mathbf{U}_k = \mathbf{U}_c + \mathbf{S}^B (\boldsymbol{\Omega}_c \times \mathbf{X}_k), \quad (\text{A.9})$$

where it should be noted that $\mathbf{S}^B \mathbf{X}_k$ is a constant vector because $\mathbf{S}^B \mathbf{X}_k$ represents a boundary point observed from Σ_B . The positions of internal Lagrangean points \mathbf{X}_{in} are also calculated in the same way as Eq. (A.8).

Appendix B. Nondimensional variables

In Section 3, we use the following nondimensional variables defined by a characteristic length H_0 , a characteristic particle speed c , a characteristic time scale $t_0 = H_0/U_0$ where U_0 is a characteristic flow speed, and a fluid density ρ_f :

$$\left. \begin{aligned} \mathbf{c}_i &= \hat{\mathbf{c}}_i/c, & \mathbf{x} &= \hat{\mathbf{x}}/H_0, & t &= \hat{t}/t_0, \\ \Delta x &= \Delta \hat{x}/H_0, & \Delta t &= \Delta \hat{t}/t_0, \\ f_i &= \hat{f}_i/\rho_f, & \mathbf{u} &= \hat{\mathbf{u}}/c, & p &= \hat{p}/(\rho_f c^2), \\ v &= \hat{v}/(cH_0), & \mathbf{g} &= \hat{\mathbf{g}}H_0/(\rho_f c^2), \\ \mathbf{X}_k &= \hat{\mathbf{X}}_k/H_0, & \mathbf{U}_k &= \hat{\mathbf{U}}_k/c, \\ \mathbf{X}_c &= \hat{\mathbf{X}}_c/H_0, & \mathbf{U}_c &= \hat{\mathbf{U}}_c/c, & \mathbf{B} \boldsymbol{\Omega}_c &= \mathbf{B} \hat{\boldsymbol{\Omega}}_c H_0/c, \\ M &= \hat{M}/(\rho_f H_0^3), & \mathbf{I}_B &= \hat{\mathbf{I}}_B/(\rho_f H_0^5), \\ \mathbf{F} &= \hat{\mathbf{F}}/(\rho_f c^2 H_0^2), & \mathbf{T} &= \hat{\mathbf{T}}/(\rho_f c^2 H_0^3), \\ \mathbf{F}_{tot} &= \hat{\mathbf{F}}_{tot}/(\rho_f c^2 H_0^2), & \mathbf{T}_{tot} &= \hat{\mathbf{T}}_{tot}/(\rho_f c^2 H_0^3), \\ \mathbf{F}_{in} &= \hat{\mathbf{F}}_{in}/(\rho_f c^2 H_0^2), & \mathbf{T}_{in} &= \hat{\mathbf{T}}_{in}/(\rho_f c^2 H_0^3), \\ \mathbf{X}_{in} &= \hat{\mathbf{X}}_{in}/H_0, & \mathbf{P}_{in} &= \hat{\mathbf{P}}_{in}/(\rho_f c), & \mathbf{L}_{in} &= \hat{\mathbf{L}}_{in}/(\rho_f c H_0). \end{aligned} \right\} \quad (\text{B.1})$$

Note that the circumflex represents ‘dimensional.’ It should be noted that the time step $\Delta \hat{t}$ is equal to the time span during which the particles travel one lattice spacing, that is, $\Delta \hat{x}/\Delta \hat{t} = c$. We can easily obtain $\Delta t = Sh \Delta x$ (where $Sh = H_0/(t_0 c) = U_0/c$) from the above relation.

In Section 4, we use the following nondimensional variables:

$$\left. \begin{aligned} D &= \hat{D}/H_0, & U_{\max} &= \hat{U}_{\max}/c, & T &= \hat{T}/t_0, & \Omega_{\max} &= \hat{\Omega}_{\max} H_0/c, & \beta &= \hat{\beta} H_0 \\ H &= \hat{H}/H_0, & \alpha_g &= \hat{\alpha}_g H_0/c^2, & u_t &= \hat{u}_t/c. \end{aligned} \right\} \quad (\text{B.2})$$

It should be noted that we can obtain $KC = \hat{U}_{\max} \hat{T}/\hat{D}$, $\hat{\beta} = (-1 + i)\sqrt{\pi/(\hat{v}\hat{T})}$ and $\Delta \theta = \hat{T} \hat{\Omega}_{\max}/(2\pi)$ by using Eqs. (B.1), (B.2), and $Sh = U_0/c$.

Appendix C. The linear momentum of the internal mass

In this section, we prove that the linear momentum of the internal mass is exactly equal to that of the rigid body with the same density of the internal mass. Let Ω be the closed domain inside the body and $\partial\Omega$ be the surface of the body. We assume an incompressible viscous fluid is filled inside Ω . Let $\mathbf{u}(\mathbf{x})$ be an arbitrary flow velocity of the internal fluid and $\mathbf{U}(\mathbf{x})$ be the velocity of the internal fluid which satisfies the rigid body motion at a point $\mathbf{x} = (x, y, z) \in \Omega$, respectively. By definition, $\nabla \cdot \mathbf{u} = \nabla \cdot \mathbf{U} = 0$ throughout Ω . We assume that the no-slip condition is satisfied on $\partial\Omega$, that is, $\mathbf{u}(\mathbf{X}) = \mathbf{U}(\mathbf{X})$ where $\mathbf{X} \in \partial\Omega$. For convenience, we define the following vector

$$\mathbf{u}' = (u', v', w') = \mathbf{u} - \mathbf{U}. \quad (\text{C.1})$$

We can readily obtain the following properties of \mathbf{u}' ,

$$\nabla \cdot \mathbf{u}'(\mathbf{x}) = 0, \mathbf{x} \in \Omega, \quad (\text{C.2})$$

$$\mathbf{u}'(\mathbf{X}) = \mathbf{0}, \mathbf{X} \in \partial\Omega. \quad (\text{C.3})$$

At first, we cut Ω by a plane $x = x_0$ which is normal to the x -axis. Let $\Gamma(x_0)$ be the cross-section surface. We consider the mass conservation in a partial domain $\Omega \cap \{x \leq x_0\}$. Because of Eq. (C.2), we have

$$\int_{\partial(\Omega \cap \{x \leq x_0\})} \mathbf{u}' \cdot \mathbf{n} dS = \int_{\Omega \cap \{x \leq x_0\}} \nabla \cdot \mathbf{u}' dV = 0. \quad (\text{C.4})$$

On the other hand, because of Eq. (C.3), we have

$$\int_{\partial(\Omega \cap \{x \leq x_0\})} \mathbf{u}' \cdot \mathbf{n} dS = \int_{\Gamma(x_0)} \mathbf{u}' \cdot \mathbf{n} dS = \int_{\Gamma(x_0)} u' dS. \quad (\text{C.5})$$

Therefore, from Eqs. (C.4) and (C.5), we obtain

$$\int_{\Gamma(x_0)} u' dS = 0. \quad (\text{C.6})$$

It should be noted that the above equation is true for an arbitrary x_0 . We can readily obtain the following equation from Eq. (C.6)

$$\int_{\Omega} u' dV = \int \left[\int_{\Gamma(x)} u' dS \right] dx = 0. \quad (\text{C.7})$$

The similar equations are obtained for v' and w' . Therefore, we conclude

$$\int_{\Omega} \mathbf{u}' dV = \mathbf{0}. \quad (\text{C.8})$$

Because the internal fluid has a uniform density, we obtain

$$\int_{\Omega} \mathbf{U} dV = V \mathbf{U}_c, \quad (\text{C.9})$$

where V is the volume of the body and \mathbf{U}_c is the velocity of the mass center of the body. By using Eqs. (C.1), (C.8), and (C.9), we have

$$\int_{\Omega} \mathbf{u} dV = V \mathbf{U}_c. \quad (\text{C.10})$$

Appendix D. Error from the no-slip condition

In order to examine the error of the no-slip condition by MDFM proposed by Wang et al. [19], we calculated the flow past a circular cylinder asymmetrically placed in a channel as shown in Fig. D.1. The diameter of the circular cylinder is D . The computational

domain is $H \times L = 22D \times 4.1D$. At the channel walls ($y = 0, H$), the no-slip condition is applied. In the inlet ($x = 0$), the following velocity conditions are imposed:

$$u(0, y) = 6\bar{U}y(H - y)/H^2, \quad (D.1)$$

$$v(0, y) = 0, \quad (D.2)$$

where u and v be the flow velocities in x and y directions, respectively, and \bar{U} is the mean velocity. In the LBM simulations, we enforce the above inlet boundary condition as follows. Let the particle velocity vectors be defined by

$$\mathbf{c}_i = \begin{cases} \mathbf{0} & (i = 1) \\ (\cos(\pi(i-2)/2), \sin(\pi(i-2)/2)) & (i = 2, 3, 4, 5) \\ \sqrt{2}(\cos(\pi(i-11)/2), \sin(\pi(i-11)/2)) & (i = 6, 7, 8, 9). \end{cases} \quad (D.3)$$

The unknown distribution functions are f_2, f_6 , and f_9 in the inlet. We assume the unknown distribution functions f_2, f_6 , and f_9 to be the equilibrium distribution function Eq. (12) with the inlet pressure $p(0, y)$ and the inlet velocity $u(0, y)$ [31]. Although the inlet pressure $p(0, y)$ is also unknown, it can be calculated from the known distribution functions and the inlet velocity $u(0, y)$ as follows:

$$p(0, y) = \frac{1}{3} \sum_{i=1}^9 f_i = \frac{1}{3} [f_1 + f_3 + f_5 + 2(f_4 + f_7 + f_8) + u(0, y)]. \quad (D.4)$$

By using $u(0, y)$ and $p(0, y)$, we calculate the unknown distribution functions f_2, f_6 , and f_9 with Eq. (12). In the outlet ($x = L$), the Neumann boundary condition is applied. In the simulation, the diameter is chosen as $D = 50\Delta x$. At the cylinder surface, the no-slip condition is enforced by the MDFM, and the number of boundary Lagrangian points is $N = 204$. Suppose that the iterative procedure in the MDFM is implemented up to ℓ times in each time step. The governing parameter of the system is the Reynolds number $Re = \bar{U}D/\nu$. We define the maximum and mean errors from the no-slip condition at the cylinder surface, E_{\max} and E_{mean} , as below:

$$E_{\max} = \frac{\max\{\|\mathbf{u}(\mathbf{X}_k)\|; k = 1, \dots, N\}}{\bar{U}} \times 100[\%], \quad (D.5)$$

$$E_{\text{mean}} = \frac{\sum_{k=1}^N \|\mathbf{u}(\mathbf{X}_k)\|}{N\bar{U}} \times 100[\%]. \quad (D.6)$$

The number of iterations ℓ in the MDFM was set to be from 0 up to 5 in order to check how E_{\max} and E_{mean} decrease as ℓ increases. In addition, we calculated the drag and lift coefficients defined as $C_D = 2F_x/(\bar{U}^2 D)$ and $C_L = 2F_y/(\bar{U}^2 D)$ (F_x and F_y are the forces acting on the cylinder in x and y directions and calculated by Eq. (7)), and examined the accuracy of the numerical method by comparing C_D and C_L with those given by Schäfer and Turek [32]. In Tables D.1 and D.2, we show E_{\max} , E_{mean} , C_D , and C_L at $Re = 20$ and 100 with the results given by Schäfer and Turek [32]. Since the flow field is

Table D.1

Comparison of E_{\max} , E_{mean} , C_D , and C_L for different numbers of iterations ($\ell = 0, 1, \dots, 5$) at $Re = 20$. The relative errors of C_D and C_L from the mean values of those given by Schäfer and Turek [32] are also shown.

ℓ	E_{\max} (%)	E_{mean} (%)	C_D	C_L
0	4.64	2.09	5.73 (2.7%)	0.0102 (−4.7%)
1	1.83	0.801	5.71 (2.3%)	0.0109 (1.9%)
2	0.945	0.402	5.70 (2.2%)	0.0111 (3.7%)
3	0.540	0.223	5.70 (2.2%)	0.0112 (4.7%)
4	0.327	0.131	5.70 (2.2%)	0.0113 (5.6%)
5	0.205	0.081	5.70 (2.2%)	0.0113 (5.6%)
Schäfer and Turek			5.58 ± 0.01	0.0107 ± 0.0003

Table D.2

Comparison of E_{\max} , E_{mean} , C_D , and C_L for different numbers of iterations ($\ell = 0, 1, \dots, 5$) at $Re = 100$. Since the flow field is time dependent at $Re = 100$, the values in this table are the maximum values for time. The relative errors of C_D and C_L from the mean values of those given by Schäfer and Turek [32] are also shown.

ℓ	E_{\max} (%)	E_{mean} (%)	C_D	C_L
0	4.06	1.47	3.43 (6.2%)	1.05 (5.0%)
1	1.61	0.562	3.36 (4.0%)	1.04 (4.0%)
2	0.833	0.285	3.33 (3.1%)	1.03 (3.0%)
3	0.480	0.164	3.32 (2.8%)	1.03 (3.0%)
4	0.293	0.104	3.32 (2.8%)	1.03 (3.0%)
5	0.249	0.072	3.32 (2.8%)	1.03 (3.0%)
Schäfer and Turek			3.23 ± 0.01	1.00 ± 0.01

time dependent at $Re = 100$, the values in Table D.2 are the maximum values for time. It should be noted that F_{in} was fairly small in the Lagrangian points approximation for both Re . Therefore, the values of C_D and C_L were independent of the schemes for approximating the internal mass effect. We can see that the error from no-slip condition is sufficiently small in the case of $\ell = 5$; the maximum error E_{\max} is less than 0.5% and the mean error E_{mean} is less than 0.1%. In addition, it can be seen that C_D and C_L are compatible with the results given by Schäfer and Turek [32]. It is noted that the small discrepancy of the present numerical results from the results given by Schäfer and Turek [32] is due to the effective radius of the sphere which is slightly larger than the input radius [5,7,30].

References

- [1] Peskin CS. Flow patterns around heart valves: a numerical method. *J Comput Phys* 1972;10:252–71.
- [2] Peskin CS. Numerical analysis of blood flow in the heart. *J Comput Phys* 1977;25:220–52.
- [3] Mittal R, Iaccarino G. Immersed boundary methods. *Annu Rev Fluid Mech* 2005;37:239–61.
- [4] Lai M-C, Peskin CS. An immersed boundary method with formal second-order accuracy and reduced numerical velocity. *J Comput Phys* 2000;160:705–19.
- [5] ten Cate A, Nieuwstadt CH, Derksen JJ, van den Akker HEA. Particle imaging velocimetry experiments and lattice-Boltzmann simulations on a single sphere settling under gravity. *Phys Fluids* 2002;14:4012–25.
- [6] Uhlmann M. An immersed boundary method with direct forcing for the simulation of particulate flows. *J Comput Phys* 2005;209:448–76.
- [7] Feng Z-G, Michaelides EE. Robust treatment of no-slip boundary condition and velocity updating for the lattice-Boltzmann simulation of particulate flows. *Comput Fluids* 2009;38:370–81.
- [8] Shen L, Chan E-S, Lin P. Calculation of hydrodynamic forces acting on a submerged moving object using immersed boundary method. *Comput Fluids* 2009;38:691–702.
- [9] Succi S. The lattice Boltzmann equation for fluid dynamics and beyond. Oxford: Oxford University Press; 2001.
- [10] Aidun CK, Lu Y. The lattice Boltzmann simulation of solid particles suspended in fluid. *J Stat Phys* 1995;81:49–61.
- [11] Inamuro T, Maeba K, Ogino F. Flow between parallel walls containing the lines of neutrally buoyant circular cylinders. *Int J Multiphase Flow* 2000;26:1981–2004.
- [12] Feng Z-G, Michaelides EE. The immersed boundary-lattice Boltzmann method for solving fluid-particles interaction problems. *J Comput Phys* 2004;195:602–28.

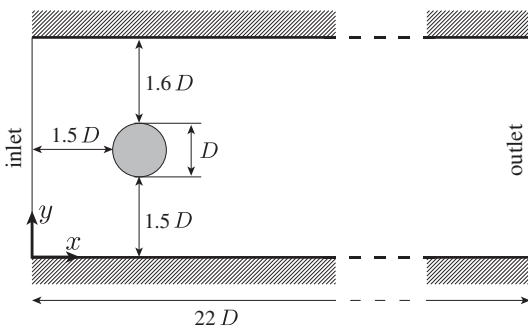


Fig. D.1. The computational domain for the flow past a circular cylinder asymmetrically placed in a channel.

- [13] Feng Z-G, Michaelides EE. Proteus: a direct forcing method in the simulations of particulate flows. *J Comput Phys* 2005;202:20–51.
- [14] Yu D, Mei R, Luo Li-Shi, Shyy W. Viscous flow computations with the method of lattice Boltzmann equation. *Prog Aerospace Sci* 2003;39:329–67.
- [15] Xia Z, Connington KW, Rapaka S, Yue P, Feng JJ, Chen S. Flow patterns in the sedimentation of an elliptical particle. *J Fluid Mech* 2009;625:249–72.
- [16] Shu C, Liu N, Chew YT. A novel immersed boundary velocity correction-lattice Boltzmann method and its application to simulate flow past a circular cylinder. *J Comput Phys* 2007;226:1607–22.
- [17] Sui Y, Chew YT, Roy P, Low HT. A hybrid method to study flow-induced deformation of three-dimensional capsules. *J Comput Phys* 2008;227:4486–98.
- [18] Wu J, Shu C. An improved immersed boundary-lattice Boltzmann method for simulating three-dimensional incompressible flows. *J Comput Phys* 2010;229:5022–42.
- [19] Wang Z, Fan J, Luo K. Combined multi-direct forcing and immersed boundary method for simulating flows with moving particles. *Int J Multiphase Flow* 2008;34:283–302.
- [20] Goldstein D, Handler R, Sirovich L. Modeling a no-slip flow boundary with external force field. *J Comput Phys* 1993;105:354–66.
- [21] He X, Luo L-S. Lattice Boltzmann model for the incompressible Navier–Stokes equation. *J Stat Phys* 1997;88:927–44.
- [22] Junk M, Klar A, Luo L-S. Asymptotic analysis of the lattice Boltzmann equation. *J Comput Phys* 2005;210:676–704.
- [23] Inamuro T. Lattice Boltzmann methods for viscous fluid flows and for two-phase fluid flows. *Fluid Dynam Res* 2006;38:641–59.
- [24] Peskin CS. The immersed boundary method. *Acta Numer* 2002;11:479–517.
- [25] Liao C-C, Chang Y-W, Lin C-A, McDonough JM. Simulating flows with moving rigid boundary using immersed-boundary method. *Comput Fluids* 2010;39:152–67.
- [26] Dütsch H, Durst F, Becker S, Lienhart H. Low-Reynolds-number flow around an oscillating circular cylinder at low Keulegan–Carpenter numbers. *J Fluid Mech* 1998;360:249–71.
- [27] Kim D, Choi H. Immersed boundary method for flows around an arbitrarily moving body. *J Comput Phys* 2006;212:662–80.
- [28] Choi J, Oberoi RC, Edwards JR, Rosati JA. An immersed boundary method for complex incompressible flows. *J Comput Phys* 2007;224:757–84.
- [29] Sherman FS. Viscous flow. McGraw-Hill; 1990.
- [30] Krüger T, Varnik F, Raabe D. Efficient and accurate simulations of deformable particles immersed in a fluid using a combined immersed boundary lattice Boltzmann finite element method. *Comput Math Appl* 2010.
- [31] Inamuro T, Yoshino M, Ogino F. A non-slip boundary condition for lattice Boltzmann method. *Phys Fluids* 1995;7:2928–30.
- [32] Schäfer M, Turek S. Benchmark computations of laminar flow around a cylinder. In: Hirschel EH, editor. Notes in numerical fluid mechanics: flow simulations with high performance computers II. Braunschweig, Germany: Vieweg; 1996. p. 547–66.